

Numerical Simulation of Receptivity of Freestream Disturbances to Hypersonic Boundary Layers with Thermochemical Nonequilibrium

Akshay Prakash* and Xiaolin Zhong[†]

UCLA, Los Angeles, CA, 90095, USA

Laminar-turbulent boundary layer transition has been studied for more than a century since Reynolds' experiments and is still poorly understood for hypersonic boundary layers. Nonlinear effects, real gas effects and receptivity processes are some of the topics that are still active areas of research. For studying hypersonic flows, inclusion of real gas effects is crucial for predicting flow parameters accurately. Real gas effects have recently been included in simulations and theoretical studies. Though there have been numerous research efforts since to simulate hypersonic flows with thermochemical nonequilibrium, there are limited numerical and theoretical studies on laminar-turbulent transition that have included thermochemical nonequilibrium. Real gas effects can radically change the receptivity process for the hypersonic boundary layer. Numerical study of unsteady flows requires high orders of accuracy to resolve vastly varying scales of space and time. Shock fitting methods can simulate hypersonic flow fields with high orders of accuracy throughout and even near the shock. Recently the authors developed a shock fitting method capable of simulating thermochemical nonequilibrium over a blunt body. This paper presents the numerical simulation of receptivity of hypersonic boundary layer with thermochemical nonequilibrium to free stream acoustic waves using the developed shock fitting algorithm. This is one of the first attempts at simulating receptivity of hypersonic boundary layer to free stream acoustic disturbances using shock fitting methodology and predicting second mode instability for real gas simulations. Test case for the current studies is based on free stream condition used earlier for experimental and numerical studies on double cone blunt bodies. Current studies predict that real gas effects destabilize the boundary layer. Real gas effects broadened the spectrum for unstable frequencies and lowered the most unstable frequency for the current case.

I. Introduction

Study and prediction of transition is very important for estimation of thermal and mechanical loading of a vehicle traveling at high speeds. Transition to turbulent flow causes a drastic increase in thermal and mechanical loads on a vehicle otherwise in a laminar regime. The accurate knowledge of onset and flow parameters of turbulent flow would help optimize the design of such an air vehicle. Bertin et al.¹ point out that vehicles powered by air breathing systems will spend most of their hypersonic flight in flow conditions that will be transitional. Flight of X15 was cited as an example where wind tunnel tests showed flow conditions to be mostly laminar but the flight tests showed that flow was mostly turbulent. The authors discussed another case of the Space Shuttle Orbiter STS-1 where design parameters computed using Aerodynamic Design Data Book (ADDB) were not correct partially due to real gas effects at very high Mach numbers. This was verified by comparing equilibrium air computations with perfect gas computations.

Transition in a boundary layer flow is a result of disturbances in the free stream or in the boundary layer in form of variation in flow field parameters or surface geometry. Reshotko² summarizes various mechanisms through which the forcing disturbances in free stream lead to turbulence (see Fig 1). Figure 1 is reproduced from Reshotko.² The green boxes and arrows in the figure show the relevant parts of the research covered

*Graduate Student, MAE, UCLA, AIAA Student Member.

[†]Professor, MAE, UCLA, AIAA Senior Member

in this study. For a flow with low disturbance levels, the process of free stream disturbances leading to turbulence is a result of T-S (Tolmein-Schlichting) waves, crossflow or Gortler mechanisms and can be split into three phases - Receptivity, the initial generation of instability waves in boundary layer, the growth of the instability waves and finally breakdown of the waves into turbulence. For larger disturbances and transient growth processes, mechanisms other than modal growth can come into play and were labeled as “bypass mechanisms”. These mechanisms are not well understood and are a topic for current research. Laminar-turbulent transition at supersonic and hypersonic speeds is complicated further by additional instability modes due to trapped acoustic disturbances.^{3,4}

Though there are engineering methods in literature which predict the onset of turbulence with varying accuracies, these are based on correlations and do not represent the physical mechanisms governing the process accurately. e^N method is the most successful method based on the assumption that transition occurs when the amplification ratio of most unstable disturbance wave attains a critical value. Theoretical studies on transition to turbulence via LST (Linear Stability Theory)^{5,6} have helped researchers in gaining vital knowledge about mechanisms leading to it. Recently, real gas effects were included in LST^{6,7} and this led to a better understanding of the process in presence of thermochemical nonequilibrium.² However complicated geometries and non-ideal behavior of air at hypersonic speeds due to high temperatures necessitate the use of numerical methods to study turbulence and mechanisms leading to it. Also LST assumes the presence of boundary layer disturbances and does not consider the receptivity process which generates the boundary layer waves as a response to the free stream forcing waves. There have been significant advances in theoretical and numerical studies for transition. These studies have been supported by experiments and flight data for the essential validation process and for valuable information on data and properties of air at high temperature conditions. DNS (Direct Numerical Simulation) is an important tool for simulation of transition phenomenon. However, currently DNS is only possible for simplistic geometries and complicated shapes are still beyond the grasp of current computational power. Fedorov⁴ gives an excellent review on developments in hypersonic flow stability and transition.

Numerical simulations complement theoretical studies and experiments by helping remove limitations of theoretical assumptions and by providing a cost effective testing bed for preliminary design. With advancement in computational power, now hypersonic flow over an air vehicle can be simulated with all the complexities of real gas effects. Modeling of hypersonic flows can be broadly classified as by shock capturing methods and shock fitting methods. Shock capturing methods are very popular owing to their robustness in capturing shocks of complicated shapes over complicated geometries including complicated shock-shock interactions.⁸ State of the art codes computing hypersonic flows with real gas effects using shock capturing ideology include LAURA code,^{9,10} DPLR code¹¹ and US3D code.¹² All the three codes are based on shock capturing schemes. A comprehensive comparison of the three codes was done earlier by Hash et al.¹³ using FIRE II¹⁴ as the test case. Recently Prakash et al.¹⁵ developed a high order shock fitting algorithm capable of simulating hypersonic flow field over blunt bodies with thermochemical nonequilibrium.

Though numerical research on turbulent and transition has been mainly done on perfect gas or ‘cold’ high speed flows, recently there have been numerous efforts to model transitional hypersonic flows accurately with real gas effects. Malik et al.⁷ solved quasi-parallel compressible linear stability equations on a mean flow with chemical equilibrium over a flat plate. They found out that for the first oblique mode at Mach 10, the growth rates are lower (similar to wall cooling effect) and peak growth takes place at a higher frequency (contrary to wall cooling effects). For the second mode instability, growth rate increased by 20% (similar to wall cooling effects) and at a lower frequency (contrary to wall cooling, suction or favorable pressure gradient). Another effect of real gas effects was to bring out a third mode of instability which was absent in perfect gas flow. For Mach 15 case there was a third mode instability in both perfect gas as well as real gas simulations, however the effect of real gas was to lower the growth rate indicating a stabilizing nature of real gas effects. Stuckert and Reed¹⁶ studied the effects of equilibrium and nonequilibrium chemical reactions on the stability of Mach 25 flow over 10° half angle sharp cone via linear stability analysis. They used shock fitting approach to eliminate spurious oscillations that could adversely affect stability analysis. They found that unlike equilibrium flow, in nonequilibrium flow the supersonic modes could not be related in a straight forward manner to the incoming and outgoing amplified solutions in the inviscid region of the shock layer. Another effect of chemical reactions was to increase the size of supersonic region by reducing temperature of the flow field and thus reducing the speed of sound. For the first mode instability the results were similar to Malik.⁷ However they did not observe a second mode instability for their test case. Johnson et al.¹⁷ compare equilibrium and nonequilibrium simulations to experimental results. They could reproduce

the general trend of increasing transition Reynolds number with decreasing dissociation energies but over predicted the transition Reynolds number by about a factor of two. Hudson et al.⁶ compared the effects of chemical equilibrium, nonequilibrium and frozen flow on transition and found that nonequilibrium does not affect transition Reynolds number for their test cases.

Ma and Zhong¹⁸ studied the receptivity of free stream disturbances of a Mach 10 nonequilibrium oxygen flow over a flat plate. They used shock fitting approach to avoid oscillations and get uniform high order accuracy for their simulations. They found that real gas effects had strong influence on second mode receptivity of reacting oxygen flow to free stream acoustic waves. They also found that unstable region for nonequilibrium flow is larger than the perfect gas flow implying the effects are destabilizing for discrete modes in the region. Stemmer et al.¹⁹ developed a hybrid method which treated shocks locally through a hybrid ENO method and other areas were dealt with compact finite difference schemes.²⁰ The authors simulated a flight case along the descent path of the space shuttle at Mach 20 (local) and altitude of 50 km and found good agreement with LST. The reacting flow was modeled using five species Park model.²¹ MacLean et al. used STABL code to compare simulations with Mach 10 flow over a 7° sharp and blunt cone and over an axisymmetric compression surface. The mean flow was obtained using DPLR code. Authors could better predict the transition location on the test cases. This was expected to help further in designing experiments to understand transition better. Leyva et al.²² used injection of CO₂ in hypervelocity boundary layers to delay transition. The experimental data was obtained from Caltech's T5 reflected shock tunnel and computations were made using DPLR (for cases without injection) and using a hybrid unstructured implicit solver.¹² The simulation results corroborated the experiments and would be used in prediction of injection schemes for new experimental cases.

Experiments related to hypersonic flow were slow to catch up with the progress in simulations primarily because hypersonic conditions encountered are extremely difficult to reproduce. A majority of computations rely on flight data for validation, like the X43 flights and FIRE flights.¹⁴ Recently built LENS facilities have the capability to fully duplicate flight conditions ranging from Mach 3 to Mach 15.²³ LENS I is capable of generating velocities up to Mach 24 for free stream conditions representing altitudes up to 90km. LENS II can generate velocities up to Mach 10 for free stream conditions for altitudes up to 70km. LENS XX is the most recent facility capable of simulating very high velocities up to 12km/s for free stream conditions up to altitudes of 80 km. None of the facilities are capable of completely creating the flow conditions for full trajectory of any of the test cases or flights; however LENS XX can reproduce the free stream conditions for most of the flight test cases like HiFIRE, RAM and FIRE. Schneider²⁴ gives an extensive survey on studies involving transition. Experiments in hypersonic boundary layer transition are limited by our ability to reproduce the flight conditions on ground testing facilities. Author discusses the need for experiments with high speed for validation of CFD methods and the need of "quite" tunnels to provide reliable validation data. Transition data from noisy tunnels may be misleading as the mechanism for boundary layer transition occurs through different mechanisms as compared to low disturbances environments encountered during actual flight.⁴ "Reentry F"²⁵ was a flight test aimed at study of turbulent heat transfer and boundary layer transition. The test case was a 5° blunted cone with 0,1 inch nose radius and 3.962m length. Free stream Mach number was 20 over altitudes of 30.48 km to 18.288 km. The authors discuss effects of detection techniques, bluntness and angle of attack. Stetson investigated transition on sharp²⁶ and blunt cones²⁷ at Mach 8 flow. Sherman et al.²⁸ performed a flight test measurement on four 22° half angle cones to get data for boundary layer transition in absence of ablative surface phenomenon. The model used a homogeneous ATJ graphite nose tip and beryllium heat shield for the main body. The cones were flown at different angle of attacks and the last cone had a spin. These measurements are important in the sense that they provide a complete set of pressure and temperature measurements from before the start of transition flow till the flow is turbulent. Hornung²⁹ measured nitrogen flow over cylinders and spheres at varying free stream conditions in large free-piston shock tunnel at physics department, ANU. The shock standoff distance was correlated to the normal shock reaction rate parameter and the curves from analytical solutions were compared with experimental results. Wen and Hornung³⁰ modified the original reaction rate parameter and included the effects of free-stream kinetic energy. They studied nitrogen, air and carbon dioxide flow over spheres. The numerical solutions were computed using Candler's code.³¹ The experiments were done at free-piston shock tunnel T5 at GALCIT. Hornung³² and Germain et al.³³ studied the effect of nonequilibrium on transition of boundary layer flows over slender cone. The authors found that nonequilibrium delays the transition significantly. Hornung³² found that the delay was due to the damping of the acoustic second mode instability by the relaxation process.

Simulation of transition and turbulence requires capturing of large range of time and length scales associated with the flow with sufficient accuracy. This requires algorithms capable of simulating the entire domain with high order of accuracy. Shock fitting approach can capture entire flow field with high order of accuracy and avoid spurious oscillations near the shock.³⁴ Zhong³⁵ developed a family of upwind compact and explicit finite-difference schemes of third, fifth and seventh order and stable high order boundary schemes for the simulation of hypersonic boundary-layer transition. The developed algorithm was extensively utilized to study receptivity by the hypersonic boundary layer^{36,37} to free stream disturbances. Later Wang and Zhong³⁸ used the algorithm extensively to study effects of surface roughness, blowing and suction on stability of hypersonic boundary layers. Ma and Zhong^{18,39} extended the algorithm to include thermochemical nonequilibrium to study receptivity of Mach 10 oxygen flow over flat plate. Recently Prakash et al.¹⁵ developed a high order shock fitting algorithm based on Zhong³⁵ capable of simulating thermochemical nonequilibrium flow with ionizing and non-ionizing models for atmospheric air over a blunt body. The algorithm includes two models for chemistry- 5 species model for non-ionizing air and 11 species model for ionizing air. The algorithm was validated over a range of free stream conditions from published simulation and experimental results.

In the current study authors use the algorithm developed¹⁵ to study receptivity of free stream acoustic disturbances by hypersonic boundary layer with thermochemical nonequilibrium. For chemical nonequilibrium 5 species air model was used. The test case is a blunt cone with nose radius of 0.25 in and half angle of 7°. Free stream condition are taken to be similar to tests computed by Olezniczak.⁴⁰ The simulations predicted destabilizing nature of real gas effects. Nonequilibrium processes broadened the spectrum of unstable frequencies and lowered the most unstable frequency. Results computed in current study are compared with previously published results on transition. There is a general agreement over destabilizing nature of real gas effects with published studies.

II. Governing Equations

Equations governing the flow are Navier Stokes equations with source terms for species and vibrational energy production. In Eq.(1) U is the vector of conservative variables. F_j is inviscid flux in j^{th} direction, F_{vj} is viscous flux in j^{th} direction and W is the source vector. These quantities are defined in Eq.(2) and (3).

$$\frac{\partial U}{\partial t} + \frac{\partial F_j}{\partial x_j} + \frac{\partial F_{vj}}{\partial x_j} = W, \quad (1)$$

$$U = \begin{bmatrix} \rho_i \\ \rho u_1 \\ \rho u_2 \\ \rho u_3 \\ E_v \\ E \end{bmatrix} \quad F_j = \begin{bmatrix} \rho_i \\ \rho u_1 u_j + p \delta_{1j} \\ \rho u_2 u_j + p \delta_{2j} \\ \rho u_3 u_j + p \delta_{3j} \\ E_v u_j \\ (E + p) u_j \end{bmatrix} \quad F_{vj} = \begin{bmatrix} \rho_i v_{ij} \\ \tau_{j1} \\ \tau_{j2} \\ \tau_{j3} \\ k_v \frac{\partial T_v}{\partial x_j} + \sum_s \rho e_{vs} D \frac{\partial c_s}{\partial x_j} \\ \tau_{ji} u_j + k \frac{\partial T}{\partial x_j} + k_v \frac{\partial T_v}{\partial x_j} + \sum_s \rho_s h_s v_{sj} \end{bmatrix} \quad (2)$$

$$W = \begin{bmatrix} W_i \\ 0 \\ 0 \\ 0 \\ Q_{T-v} + \sum_s e_{vs} \\ 0 \end{bmatrix} \quad (3)$$

In the above mentioned equations, subscript j is the direction, i and s denote species v denotes vibration and c stands for mass fraction of species. For current simulations we use Blottner's⁴¹ curve fit for transport coefficients, Park's²¹ rate constants for chemical source terms, 5 species model for chemistry and Park's⁴² two temperature model for thermal nonequilibrium. For more details about the method the reader is referred to Prakash et al.¹⁵

III. High Order Shock Fitting Method for Nonequilibrium Hypersonic Flow Over Blunt Bodies

The high order shock fitting method is based on the shock fitting method derived by Prakash et al.¹⁵ Navier-Stokes equations are discretized on the domain between the shock and blunt body and solved numerically. Due to the presence of subsonic region in front of the blunt body the governing equations become elliptic. The convection terms are grouped together as inviscid terms and solved using flux splitting methods while the diffusion terms are grouped as viscous terms and solved using high order central discretization. The source terms are put separately in W . These equations are transformed to body fitted coordinates, symbolically denoted by Eq.(4)

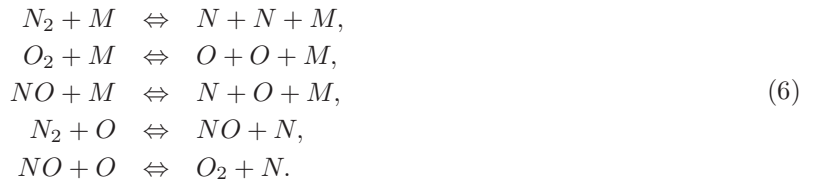
$$\begin{cases} \xi = \xi(x, y, z) \\ \eta = \eta(x, y, z) \\ \zeta = \zeta(x, y, z) \\ \tau = t \end{cases} \iff \begin{cases} x = x(\xi, \eta, \zeta, \tau) \\ y = y(\xi, \eta, \zeta, \tau) \\ z = z(\xi, \eta, \zeta, \tau) \\ t = \tau \end{cases} \quad (4)$$

$$\frac{1}{J} \frac{\partial U}{\partial \tau} + \frac{\partial E'}{\partial \xi} + \frac{\partial F'}{\partial \eta} + \frac{\partial G'}{\partial \zeta} + \frac{\partial E'_v}{\partial \xi} + \frac{\partial F'_v}{\partial \eta} + \frac{\partial G'_v}{\partial \zeta} + U \frac{\partial \frac{1}{J}}{\partial \tau} = w \quad (5)$$

For the inviscid terms a fifth order upwind scheme developed by Zhong³⁵ is used with Local Lax Friedrich flux splitting. For viscous terms sixth order central scheme is used for discretization. At the shock the boundary conditions are computed by Rankine Hugoniot relations. The shock velocity is computed using the compatibility relations immediately behind the shock. The reader is referred to Zhong³⁵ and Prakash et al.¹⁵ for more details.

IV. Five Species Air Model

For the current study, basic five species air model was used to represent chemical nonequilibrium. The five species air model consists of N_2 , O_2 , NO , N , O . As the air crosses the shock and encounters high temperatures, oxygen starts dissociating. The atomic oxygen reacts with nitrogen to form NO . This is represented by the last two Zeldovich reactions in Eq.[6]. As the temperature rises above 3000K, oxygen is completely dissociated and nitrogen starts dissociating. Nitrogen almost completely dissociates by the time temperature reaches 9000K. For the test case in current study the flow-field temperatures remain below 9000K and ionization is not expected. This is corroborated by the current simulations. The five species model consists of the following reactions³¹



For reaction rate constants and more details, the reader is referred to Candler³¹ or Prakash et al.¹⁵

V. Vibration Energy

As the temperature rises above about 3000K, additional modes of energy for molecules become excited. Rotation mode is assumed to be equilibrated with the translation mode for temperatures of interest (characteristic rotation temperature for N_2 , for example, is about 3 K). For the current study it is assumed that all diatomic species are governed by a single vibration-electronic temperature. This means that the relaxation time for vibration energy of different diatomic species to become equilibrated with each other and with electronic energy is much smaller than the translation-vibration relaxation. This implies that a common governing equation for vibration energy can be used for all species. For more details about the vibration energy equations and species constants used, the reader is referred to Prakash et al.¹⁵

VI. Free Stream Disturbances

Free stream disturbances can be classified as acoustic, entropy or vorticity waves. Equations [8], [9], [10] and [11] give the values of free stream parameters perturbed for introducing each of the mentioned disturbances.⁴³

Fast Acoustic Waves:

$$\begin{aligned}
 \omega &= k_{\infty} \left(\frac{1}{M_{\infty}} + \cos \theta_{\infty} \right), \\
 |u'|_{\infty} &= \epsilon \cos \theta_{\infty}, \\
 |v'|_{\infty} &= -\epsilon \sin \theta_{\infty}, \\
 |p'|_{\infty} &= \epsilon \gamma M_{\infty}, \\
 |\rho'|_{\infty} &= \frac{|p'|}{\gamma},
 \end{aligned} \tag{7}$$

Slow Acoustic Waves:

$$\begin{aligned}
 \omega &= k_{\infty} \left(\frac{-1}{M_{\infty}} + \cos \theta_{\infty} \right), \\
 |u'|_{\infty} &= -\epsilon \cos \theta_{\infty}, \\
 |v'|_{\infty} &= \epsilon \sin \theta_{\infty}, \\
 |p'|_{\infty} &= \epsilon \gamma M_{\infty}, \\
 |\rho'|_{\infty} &= \frac{|p'|}{\gamma},
 \end{aligned} \tag{8}$$

Entropy Waves:

$$\begin{aligned}
 \omega &= k_{\infty} \cos \theta_{\infty}, \\
 |u'|_{\infty} &= 0, \\
 |v'|_{\infty} &= 0, \\
 |p'|_{\infty} &= 0, \\
 |\rho'|_{\infty} &= \epsilon M_{\infty},
 \end{aligned} \tag{9}$$

Vorticity Waves:

$$\begin{aligned}
 \omega &= k_{\infty} \cos \theta_{\infty}, \\
 |u'|_{\infty} &= \epsilon \sin \theta_{\infty}, \\
 |v'|_{\infty} &= \epsilon \cos \theta_{\infty}, \\
 |p'|_{\infty} &= 0, \\
 |\rho'|_{\infty} &= 0,
 \end{aligned} \tag{10}$$

Note that acoustic waves propagate with speed of sound with respect to the flow, vorticity and entropy waves propagate with the flow velocity. Also note that acoustic waves are isentropic whereas entropy waves are not. Fast acoustic disturbances were imposed on the free stream with sixteen discrete frequencies varying linearly. Free stream disturbances are represented by

$$q_{\infty}(x, y, t)' = \sum_n |q'_{\infty n}| \exp i k_{n\infty} (x - c_{\infty} t), \tag{11}$$

where q_{∞} represents perturbation of a flow variable, $|q'_{\infty n}|$ is the amplitude, k_{∞} is the wavenumber, and c_{∞} is the phase speed of the disturbance wave in the free stream before reaching the shock. The free stream acoustic wave data is shown in table 1. Note that ϵ in table 1 is the amplitude of nondimensional $|q_{\infty}|$ (nondimensionalized by free stream value of the corresponding variable).

Table 1. Free stream disturbance.

f	$28.44 - 455.04kHz$
ϵ	0.0005

VII. Boundary Condition

The computational domain used for the study has four boundaries (Fig. 2). The boundary at the shock is computed using Rankine-Hugoniot normal shock relations. For species mass fractions frozen flow is assumed across the shock and the mass fractions of the species are taken to be the same as free stream values. The cases in current paper fall well within the continuum range and the thin shock assumption and frozen flow assumption across the shock are valid. For the present cases a non-catalytic surface with temperature specified boundary condition is used. The vibration temperature is assumed to be equal to translation temperature at the wall. Pressure is extrapolated using a high order polynomial from the flow field. For the test cases considered in this study no slip conditions at the surface are appropriate due to the assumption of thermodynamic equilibrium of the fluid with the surface. For rarefied gas flow, for example, the use slip boundary conditions would be necessary because the fluid is no longer in thermodynamic equilibrium with the surface. For a blunt cone there is a singularity at the stagnation line, due to the computational domain chosen, for evaluation of grid Jacobians. This region is not included in the computations and is extrapolated from the flow field solutions using high order polynomial curve fit. The supersonic flow at the exit boundary allows the use of extrapolated values using polynomial curve fits.

VIII. Receptivity of Mach 5.71 Flow over Blunt Cone

This case for unsteady simulations is based on one of a series of experiments performed at T5 shock Tunnel at California Institute of Technology.⁴⁰ Olejniczak⁴⁰ designed experimental test cases which were not easy to reproduce computationally. These cases were nitrogen flow over double cone geometry. The test conditions for current simulations are from shot 1035.⁴⁰ This case was chosen because it is a high enthalpy case and unlike Lobb's⁴⁴ Mach 15.3 case (which is also a very good candidate as a test case for simulation of nonequilibrium process) it has relatively lower free stream Mach number of 5.71. This facilitates the use of smaller grid for computations. In the current study the free stream conditions are changed to air instead of nitrogen. Study of transition with air as a medium makes more sense than nitrogen because it is air where the actual flights take place. Also considering air as a medium is more appropriate for real gas effects as it consists of oxygen which dissociates at a much lower temperature than nitrogen ensuring real gas effects in far downstream region away from stagnation when temperatures wont be as high. Free stream conditions for this test case are listed in Table 2. The cone is at a half-angle of 7° with the horizontal with a blunt nose (nose radius equal to quarter of an inch). Simulations of real and ideal gas models are compared.

Table 2. Free stream conditions for Mach 5.71 case.

P_∞	5080Pa
$T_{v\infty}$	4137[K]
ρ_∞	$6.6 \times 10^{-3}[kg/m^3]$
N_2	0.655
O_2	0.0001
NO	0.0
N	0.135
O	0.2099
Mach number	5.71

A. Mean FLOW

Real gas simulations were computed for a domain length of 2.5m to get second mode instability. This is a very long computational domain. The domain was computed by breaking it into smaller zones partly because the location of instability is not known a priori and mainly because the domain is too large to be computed as a whole due to memory restrictions. Ideal gas simulations were computed later to match the zones in terms of location and extent for comparison.

Computations domain for the first zone is shown in Fig. 3. The black line is the surface. The region shaded in gray is the cone. On the right where the mesh ends and no boundary is shown is the exit. At the surface temperature and vibration temperature are fixed at 1000K, pressure is extrapolated and species have zero mass fraction gradient corresponding to non-catalytic wall. Since the flow is supersonic at the exit boundary except for a small region near the wall, the flow variables are extrapolated using high order polynomial curve fit. At the shock the flow variables are computed using Rankine-Hugoniot relations. Vibration temperature and species mass fractions are frozen across the thin shock. The case was computed on 7840x180 grid for ideal gas and 9440x180 grid for real gas runs.

Due to sharp rise in translation-rotation temperature across the shock, species become out of equilibrium. For real gas simulations, thermochemical relaxation reduced the temperatures in the flow field. For ideal gas runs, the chemical and vibration source terms are neglected. Hence there is no thermochemical relaxation for ideal gas runs and the temperatures remain high. The difference in temperatures (and hence in density) causes the shock standoff distance to be much smaller for real gas computations as compared to ideal gas simulations. Figures 4 and 5 compare shock standoff distance between ideal and real gas computations. Figure 4 shows shock standoff distance for stagnation region. Green line (lighter) is for ideal gas computations and red (darker) line for real gas computations. As discussed above, for ideal gas simulations the shock standoff distance is about double as that for real gas simulations. However, downstream of the stagnation region, shock is oblique and temperature rise is not as high as stagnation. The dissociated flow from stagnation region starts recombining (essentially N combining to form N_2) increasing the temperature in the flow field. This causes the shock standoff distance to increase for real gas. Figure 5 compares shock standoff for the flow field further downstream. The red (darker) line (real gas shock) crosses the green (lighter) line (ideal gas shock), surpassing it in terms of distance from the surface. This reversal in shock standoff distance for real and ideal gas simulations is not usual because most of the test cases do not have high temperatures in the free stream (and hence gas is not in dissociated form like the present test case). The inverted curvature of the shock is peculiar to this test case and may have some effects on the receptivity process.

For real gas simulations, chemical and thermal relaxation distribute the flow energy more evenly over other modes (namely the chemical and thermal modes) causing a lower temperature in the flow field near stagnation region. Figure 6 compares temperature profiles for ideal and real gas computations at stagnation line. The maximum translation temperatures reached are about 18000K behind the shock reducing to 1000K at the surface. For ideal gas the translation-rotation temperature remains at 18000K for most of the region while for real gas the temperature falls sharply behind the shock due to thermochemical relaxation process. The vibration temperature starts at about 4137K - the free stream value. This is because it is assumed that vibration temperature (along with species mass fractions) remains frozen across the thin shock. For ideal gas the vibration temperature remains at this value for most of the flow field reducing to 1000K at the wall. For real gas simulations, the vibration temperature rises quickly due to thermal relaxation and remains at about 9000K for most of the flow field dropping down to 1000K at the wall. Since the temperature for real gas remains at about 9000K for most of the flow field, the real gas models used are valid for the test case. Figure 7 compares temperature contours for ideal and real gas computations in the stagnation region. Real gas simulations are represented by half cone at the top and ideal gas by half cone at the bottom. For ideal gas computations the temperature remains high in the stagnation region. Downstream over the sphere temperature falls and remains low for remaining flow field as shown by bottom cone in Fig. 8. For real gas simulations the temperature rises across the shock but for most of the stagnation region the temperature is lower than the ideal gas case at about 9000K. Temperatures drop downstream of the stagnation region and are lower than ideal gas predictions. This can be seen by the darker shades of blue contours for real gas cone (top) as compared to the slightly lighter shades for ideal gas cone (bottom) away from the stagnation in Fig. 7. Further downstream the temperature increases for real gas simulations due to recombination of chemical species while for ideal gas predicted temperatures remain low throughout. This can be seen in the plots by the lighter shade of blue contour lines for real gas cone (top) as compared to darker blue for ideal

gas cone (bottom).

Vibration temperature varies like translation-rotation temperature due to thermal relaxation. Note that vibration temperature remains frozen across the thin shock. Figure 9 shows contours for vibration temperature near stagnation region (top) and the flow field (bottom) for real gas simulations. Immediately behind the shock vibration temperature is at its free stream value due to frozen flow assumption. Thereafter it rises sharply to about $9000K$ due to relaxation process falling to $1000K$ at the surface. Away from the stagnation region, vibration temperature decreases like the translation temperature. Note that the free stream value of vibration temperature is much higher than free stream value of translation temperature. Further downstream the vibration temperature is almost at about $4000K$ except near the surface where it drops to $1000K$. In the region where the shock is not strong and translation temperature is lower than the vibration temperature, thermal relaxation tends to increase translation temperature at expense of vibration temperature, though the change in temperature due to the relaxation process is very small.

Variation in temperatures has a direct effect on mass fraction of species. Diatomic nitrogen, atomic nitrogen and atomic oxygen constitute the dominant species in the flow field. Figure 10 shows contours for N_2 mass fractions near stagnation region and in the flow field for real gas simulations. Top figure shows contour lines near stagnation region and the bottom figure shows contour lines for the flow field. Due to high temperatures in the stagnation region N_2 dissociates. The minimum mass fraction for N_2 is near the surface at stagnation region visible in the plot as dark blue contour lines (top figure). The streak of low concentration for N_2 vanishes downstream of the stagnation region. The plot for the flow field (bottom figure) show increasing mass fraction contours further downstream of the cone. This is due to recombination of N atoms to form N_2 . This is the reason for increase in temperature for real gas simulations downstream and hence an increase in shock standoff distance shown in Fig. 5

Unlike nitrogen and atomic oxygen, NO and diatomic oxygen are present in very small amounts for most of the flow field. Temperatures are high enough for diatomic oxygen to dissociate. Hence, for most of the flow field oxygen remains in the atomic state. Mass fractions of oxygen and NO do not vary by significant amounts away from the stagnation region. Near the stagnation region nonequilibrium effects are strong and even these species with low mass fractions show significant variations. Figure 11 shows contours of NO (top) and O (bottom) mass fractions near stagnation region for real gas simulations. Mass fractions for NO are low throughout the flow field except near the stagnation region. Slightly away from the stagnation line a thin area of high mass fraction of NO is visible which decays quickly downstream of the spherical nose region. Note that NO has low concentrations at very high and very low temperature values. The figure also shows O mass fractions. Due to high vibration temperature in the free stream and low dissociation energy of O_2 , O has high mass fractions throughout the flow field except for a thin region near the stagnation where NO mass fractions are high. Further downstream O mass fractions again increase as NO dissociates. Note that mass fractions for O_2 are set to be negligible in the free stream.

As discussed earlier, variation in temperatures has a direct effect on variation in mass fractions. Near the stagnation region where the nonequilibrium effects are the strongest, the variation in species mass fractions is the highest. Figures 12 show the variation of mass fractions of species along the surface for the computational domain. The x coordinate in the figure (S_x) is distance from the stagnation point measured along the surface of the cone in meters. The figure on top shows the variations near the stagnation region. Due to high temperatures in the stagnation region mass fractions of diatomic oxygen remain low. A substantial amount of N_2 is dissociated and along with O and N constitutes the major species in the flow field. Near the stagnation region, due to higher temperatures as compared to the flow downstream, mass fractions of N_2 decrease and that of N increases. However as is shown in Fig. 12 (bottom), mass fractions of N_2 increase as those of N decrease downstream of the domain. This is due to recombination reactions, also increasing the temperature of the flow field. The mass fractions of O_2 increase as well indicating recombination of atomic oxygen. Mass fractions of NO remain low throughout the flow field.

Variation of species mass fractions across the flow field is also highest in the stagnation region and decreases downstream of the stagnation region in accordance with the variation in temperatures. Figure 13 shows profiles for mass fractions of species across the flow field for selected locations in the computational domain. Near the shock the mass fractions are set to be the same as free stream values. Mass fractions of N_2 decrease towards the surface and those of N increase, reaching a minimum near the boundary layer edge (and maximum for N) and increasing again at the surface. This variation is in accord with variation in temperatures shown in figure 14 for $x = 0.005576$. Vibration temperature is highest at near the edge of the boundary layer. Though temperature decreases steadily from shock to surface, dissociation reactions

for N_2 and O_2 depend on average of vibration and translation temperature. Variation in mass fractions of other species is not as significant as the variation of mass fractions of N_2 and N . Further downstream as the boundary layer grows and temperatures are steady, mass fractions become steady. Slight variation in mass fraction of species is noticeable as a small slope in lines from shock to surface. However there is significant variation in mass fractions of N_2 and N in the boundary layer at $x = 0.08m$ (as there is a significant variation of temperatures in the boundary layer). Further downstream variations in mass fractions (and in temperatures) decreases. The mass fractions of N_2 and N are significantly different from free stream at the wall near the stagnation region. Towards the exit of computational domain the mass fractions of N and N_2 come closer to the free stream value.

Boundary layer profiles for temperature show larger boundary layer thickness for real gas simulations near the stagnation region. Away from the stagnation region, the boundary layer thickness is similar for ideal and real gas simulations. However, the profiles for temperatures are not the same for ideal and real gas simulations. Figures 14 and 14 show boundary layer profiles for temperatures at a number of x locations starting from near the stagnation region to the end of the computational domain. Near stagnation region at $0.008m$ translation temperature has a lower slope at surface and lower value in the free stream for real gas simulations due to chemical reactions and thermal relaxation. Vibration temperature which has a higher value in free stream due to flow from upstream and due to relaxation has about the same slope as the ideal gas translation temperature. Further downstream at $0.08m$, translation temperature for real and ideal gas have similar values near the shock. For real gas the temperature falls as the mixture reacts and has a lesser slope at surface compared to ideal gas case. Vibration temperature is the highest due to flow from upstream and higher value in free stream. Further downstream, real gas translation temperature is higher than ideal gas translation temperature near the shock due to thermal relaxation and has similar value as the ideal gas temperature near the surface due to lower effects of chemical reactions. The rise in value near the surface is due the viscous dissipation. Vibration temperature which has a higher value in the free stream falls slightly towards the surface to rise again due to thermal relaxation at the wall and fall back to surface temperature at the wall.

B. Unsteady Solutions

Once steady solutions are computed, unsteady flow is computed by introducing forcing waves in the free stream. As discussed earlier, free stream perturbations can be acoustic, entropy or vorticity waves. For the current study, the free stream was perturbed with fast acoustic waves of 16 frequencies varying linearly from 28.44 kHz to 455.04 kHz. The phase angle of the perturbations in free stream for all frequencies were randomly chosen and all the frequencies had equal amplitudes. The unsteady flow field was computed for an interval of few time periods of the forcing waves till the flow stabilized. The unsteady solution was analysed using Fast Fourier Transforms to separate various modes and their amplitudes. For FFT analysis, flow variables are saved for $2n$ intervals in time, where n is the number of representative frequencies.

1. Unsteady Perturbations

Perturbed values of the flow variables can be obtained by subtracting the steady computations (mean flow) from unsteady computations. Contours for perturbed flow variables for real gas simulations are presented in Fig. 15, Fig 16 and Fig 17. Note that perturbations in these contours is sum of 16 frequencies corresponding to the 16 frequencies used in forcing waves in the free stream. Also note that perturbation variables are nondimensionalized by values of corresponding mean variables in the free stream.

The flow field can be divided into two main wave regions- boundary layer and the inviscid flow field. It was shown by Zhong⁴⁵ that for a compressible flow around a blunt body with shock, the flow field disturbances are complex response to a combination of free stream forcing and boundary layer waves. Figure 15 shows contours of pressure perturbations for real gas simulations. In the region that is still very close to the nose, the waves are not completely formed; however a formation of waves at the surface can be seen. Also noticeable is the discontinuity across different zones. This is expected since different zones have different intervals of simulation time due to different time-steps based on CFL condition. Figure 16 shows contours of temperature perturbations for real gas simulations. Here too waves are not well formed, but visible faintly are small wave patterns at the surface. In Fig. 15 and Fig. 16 wave formations near the shock are distinctly different from those in the boundary layer. The wave formations in the middle region of the flow field seem to come off the boundary layer, but the wavelength is similar to those near the shock showing the influence of

both boundary layer waves and free stream disturbances. Figure 17 shows contours of oxygen mass fraction perturbations for real gas simulations. Complex wave structures in the flow field are visible which are like free stream forcing waves (waves near the shock) except near the boundary where they are similar to the boundary layer waves. Note that for fast acoustic disturbances, temperature is not perturbed in the free stream.

Perturbations obtained by subtracting mean flow from unsteady flow are superposition of 16 frequencies imposed in the free stream. Contours for perturbations for a specific frequency can be plotted by plotting real part of perturbation data obtained after FFT analysis. Figure 18 compares instantaneous pressure perturbations (nondimensionalized by free stream pressure) for frequency $n=11$ ($f=312.84$ kHz) for ideal and real gas simulations (side by side). Note that frequency $n=11$ is second mode unstable for both ideal and real gas simulations. In Fig. 18(a), near the stagnation region, the perturbation contours are very different for ideal and real gas indicating substantial real gas effects. Wave structures are not formed yet but the difference in contour formation near the edge in Fig. 18(a) and Fig. 17(c) is noticeable. Figures 17(e) and 17(f) show formation of waves further downstream. The boundary layer waves are well formed and prominent. Waves near the shock are also visible though not as strong as boundary layer waves. In Fig. 18(g) and Fig. 18(h) to Fig. 18(q) and Fig. 18(r), the contours for ideal and real gas cases are similar indicating that for pressure perturbations the real gas effects are not significant. The waves are well formed. Waves from the shock show a distinct structure different from the boundary layer disturbance waves. Figures 18(g) and 18(h) show strong waves near the surface and boundary. The waves in the flow field are not as strong. Also note that for ideal gas (Fig. 18(h)) the perturbations near the shock are more stronger than those for real gas (Fig. 18(g)). Downstream the waves in the flow field grow stronger as shown in figures 18(i)- 18(l). Figures 18(q) and 18(r) show strong waves in the flow field and weaker waves in the boundary layer and near the shock. However the strength of the perturbation waves in flow field decreases from Fig. 18(m) to Fig. 18(r). This is because the strength of boundary layer waves increases (Note that the contour levels remain almost the same). In the last two figures (one each for real gas and ideal gas simulations) strong boundary layer perturbations are distinctly visible. Fig. 18(u) and Fig. 18(v) compare the last two zones for ideal gas simulations with the corresponding zones for real gas simulations. Contours are different for real and ideal gas simulations for this zone. Figures 18(s) and 18(u) both show strong growth of boundary layer towards the exit of the zone. For ideal gas simulation, only zone 13 (Fig. 18(v)) shows the strong second mode growth of boundary layer disturbances. A (Fig. 18(t)) strong disturbance growth was observed near the shock which decayed downstream (Fig. 18(v)). This may not be physical and be due to unresolved flow field near the shock. In the sequence of figures for ideal gas simulations from zone 7 to zone 12, boundary layer perturbations and perturbations near shock causing strong perturbations in the flow field can be noticed. These strong perturbations later shift very close to the boundary layer. Shortly thereafter strong second mode growth in the boundary layer is observed.

For real gas simulations, N_2 , N and O are the dominant species in the flow field. Comparison between real and ideal gas simulations for species mass fractions would not make sense because chemical source terms are neglected in ideal gas simulations. Species mass fraction perturbations would be same as density perturbations. Contours of N and O mass fraction perturbations for real gas simulations are presented next. Figures 19(a) to 19(r) show contours for mass fraction perturbations of N for the flow field. Fig. 19(a) and Fig. 19(b) show N mass fraction perturbations for first two zones. Boundary layer is very thin and can be noticed by careful examination of contours near the surface. Note that stagnation region is the region where nonequilibrium effects are prominent.

Over the next few zones, boundary layer develops and perturbation contours start forming into visible patterns. Note that zones 3, 4 and 5 are combined as one zone 3. Figure 19(c) shows perturbation contours for zone 3. Boundary layer grows visibly large in this zone and waves are clearly visible. Waves near the shock and in the boundary layer are distinctly different, developing over the zone. Discontinuity in contours are visible in the figure due to overlap of different zones. Figure 19(d) shows perturbation contours for zone 6. The figure shows waves near the shock and in the boundary layer and waves developing in the flow field towards the end of the zone because of the forcing of these two (boundary layer waves and waves near the shock) disturbances. Also noticeable is the growth of boundary perturbations and perturbations near the shock. Figures 19(f) show N mass fraction perturbations contours for zone 7. Strong perturbations near the shock and not as strong perturbations near the boundary layer are visible. Waves develop in the flow field as a response to forcing due to these two disturbances. Perturbations in the flow field grow stronger towards the exit of the zone. Figure 19(f) shows contours near the surface. The figure shows boundary layer

waves giving rise to waves in the flow field and interact with the disturbances from the shock. Figures 19(g), 19(i), 19(k) and 19(l) shows N mass fraction perturbation contours for zone 8, zone 9, zone 10 and zone 11. The plots show three distinct waves- near the shock, in the flow field and near the boundary. The waves are well developed. The later zones show more waves in the flow field as the shock standoff distance increases. Disturbances are stronger near the shock and in the flow field than in the boundary. Figure 19(m) shows contours for N mass fraction perturbations for zone 12. Strong group of waves near the shock, in the flow field and near the surface are visibly separated by weaker disturbances. Perturbations in the flow field and near the shock are stronger than those in the boundary layer. Figure 19(n) shows N mass fraction perturbations near surface for zone 12. Boundary layer disturbances interact with much stronger disturbances from the flow field. Figure 19(o) shows contours for N mass fraction perturbations for zone 13. Perturbation in boundary layer grow causing contours for perturbations in the flow field and near the shock to appear weaker. Strong perturbations branching off the boundary layer are visible near the exit of the domain shown. Figure 19(p) shows the strong perturbation contours near the surface. Figure 19(q) shows contours for zone 14. Boundary layer disturbances grow stronger suppressing the disturbance contours in the flow field and near the shock. Note that this is the last zone computed. Computations in next zone are unstable due to the large perturbations in the boundary layer.

2. FFT Analysis

The computed unsteady solution was analyzed via Fast Fourier Transforms (FFT). The FFT algorithm is base on Danielson-Lanczos formula from Numerical Recipes.⁴⁶ Perturbations in 16 different frequencies were imposed in the free stream. The perturbations in the flow field are decomposed into the same sixteen frequencies. At the end of FFT analysis, amplitudes and phase angles of the perturbations in each frequency are known. The perturbations in the flow field can be represented by

$$q' = |q'| \exp i|\psi - \omega t| \quad (12)$$

for each frequency. Angular frequency ω^* can be computed from frequency f^* using

$$\omega^* = 2\pi f^*. \quad (13)$$

Note that * quantities are dimensional. Nondimensional frequency F and angular frequency ω can be computed from nondimensional quantities using

$$F = \frac{\omega^* \mu_\infty^*}{\rho_\infty^* u_\infty^{*2}}, \quad (14)$$

and

$$\omega = RF, \quad (15)$$

where R is the Reynolds number based on a length, characteristic of the boundary layer thickness computed by

$$R = \frac{\rho_\infty^* u_\infty^* S}{\mu_\infty^*}, \quad (16)$$

where L^* is the characteristic length computed by

$$L^* = \sqrt{\frac{\mu_\infty^* S^*}{\rho_\infty^* U_\infty^*}}, \quad (17)$$

where S^* is the natural length measured from the stagnation point.

Growth rate is defined as

$$\alpha_i = \frac{d}{dS} |q_n| / |q_n|. \quad (18)$$

Streamwise wavenumber can be computed by

$$\alpha_r = \frac{d}{dS} |\phi_n|, \quad (19)$$

and finally the phase speed of the disturbance can be computed by

$$a = \frac{\omega_n}{\alpha_r}. \quad (20)$$

Phase speed diagrams are very helpful way of showing whether the fast acoustic disturbances have synchronized with the unstable Mack modes or not. As mentioned above, disturbances can be acoustic, entropy and vorticity waves. Fast acoustic waves travel with phase velocity of $(1 + \frac{1}{M_\infty})$, entropy and vorticity waves with phase velocity of (1) and slow acoustic waves with phase velocity of $(1 - \frac{1}{M_\infty})$.³⁶ Fast acoustic waves are excited near the stagnation region due to free stream forcing waves. The phase velocity of these waves decreases downstream of the nose region (see Fig. 20). These disturbances were called mode I, mode II and so on in the order they appeared.³⁶ When the wave speeds reduces such that these modes are in synchronization with Mack modes,⁵ they excite these modes. Mode I and these family of modes are stable, but initially grow due to forcing from the free stream disturbances and eventually decay. When the unstable Mack modes are excited, they tend to grow because they are inherently unstable. Amplification of these Mack modes eventually leads to turbulence. Often the modes are excited due to free stream perturbations and tend to exhibit wave like patterns due to overriding waves of different wavelengths. Note that for figures showing amplitudes of perturbations, the amplitudes are nondimensionalized by corresponding free stream values.

The flow field was perturbed with 16 frequencies (28.44 kHz - 455.04 kHz). Amplitudes for perturbations from FFT (Fast Fourier Transform) analysis for pressure perturbations for ideal gas runs are shown in Figure 21 for frequencies n=1 (f=28.44 kHz) to n=6 (f=170.64 kHz). The free stream acoustic perturbations generate waves in the flow field which are strongest at the stagnation region and rapidly decay over the spherical nose. Over the cone the amplitudes gradually increase for this frequency range. The amplitudes increase gradually and would decrease till they reach the synchronization point where they excite the unstable Mach modes. For the frequencies shown, exponential growth was not observed for the current test case indicating that the synchronization point has not been reached. Frequency n=1 shows the slowest growth and n=6 shows highest growth, decaying in wave like manner after reaching peak.

For real gas simulations, pattern for the amplitude growth is similar to ideal gas case. Figure 22 shows amplitudes of pressure perturbations for frequencies n=1 (f=28.44 kHz) to n=6 (f=170.64 kHz) for real gas simulations. Frequencies n=5 (f=142.2 kHz) and n=6 show initial growth and then decay towards the end. Frequencies n=1 to n=4 (f=113.76 kHz) show small growth for the computed domain. However like ideal gas case none of the frequencies have reached the synchronization point.

Amplitudes of pressure perturbations for frequencies n=6 (f=170.64 kHz) to n=11 (f=312.84 kHz) are shown in Figure 23 for ideal gas runs. All the frequencies shown follow a wavy pattern. None of the frequencies shown in the figure except n=11 have reached synchronization point and hence none are expected to show a second mode growth. For frequencies n=6 and n=7 (f=199.08 kHz) it is not evident whether they grow or decay. However phase velocity plots (discussed later) do not show synchronization point for this frequency. For frequencies n=8 (f=227.52 kHz) and n=9 (f=255.96 kHz), if an envelop is constructed over the waves, the pattern will be shown to be decaying. For frequency n=10 (f=284.40 kHz) the envelop would first decay and then again grow towards the end of the plot. However, as phase velocity plots indicate (discussed later), none of these frequencies reach synchronization point of the domain simulated. Hence second mode growth is not expected for these frequencies. Frequency n=11 (f=312.84 kHz) shows exponential growth (discussed later). The phase velocity plots show synchronization point for the frequency at this location.

For real gas simulations, second mode instability was observed in the range n=8 (f=227.52 kHz) to n=11 (f=312.84 kHz). Figure 24 shows amplitudes of pressure perturbations for frequencies n=6 (f=170.64 kHz) to n=11 for real gas simulations. Note that y axis is shown in log scale. The exponential growth is not as pronounced as in linear scale plots. The plot shows frequencies n=8, n=9 (f=255.96 kHz), n=10 (f=284.40 kHz) and n=11 growing exponentially. These are second mode unstable frequencies for this test case. Frequency n=11 starts the exponential growth first (location of synchronization point, 1.524m) followed by n=10 (1.715m), n=9 (1.905m) and n=8 (2.16m). Synchronization point for lower frequencies not showing the second mode growth is further downstream. Flow further downstream needs to be computed to find out the range of unstable frequencies (the Mack modes). The largest growth rate is by n=9, although n=8 shows a similar growth for the range it grows.

Ideal gas simulations show instability for frequency n=11 (f=312.84 kHz). All other frequencies are stable. Figure 25 shows amplitudes of pressure perturbation for ideal gas simulations for frequencies n=11 to n=16 (f=455.04 kHz). Frequencies in this plot also show a wavy pattern decaying after a rapid initial

growth and gradually growing again towards the end. Frequencies $n=11$, $n=12$ ($f=341.28$ kHz) and $n=13$ ($f=369.72$ kHz) seem to grow rapidly towards the end. However only frequency $n=11$ shows second mode growth. This is also demonstrated in a later plot comparing amplitudes for pressure perturbations for $n=11$ ideal and real gas simulations. Ideal gas case could not be computed beyond 2.2m (as opposed to 2.5m for real gas) due to instabilities at the shock. The instabilities are visible in Fig. 18 near the shock towards the exit where contours show rapidly growing disturbances. It is believed that this growth is due unresolved flow at the shock.

Amplitudes of pressure perturbations for frequencies $n=11$ ($f=312.84$ kHz) to $n=16$ ($f=455.04$ kHz) are shown in Fig. 26 for real gas simulations. Except $n=11$, which grows exponentially, all other frequencies in the plot decay after a brief growth displaying wavy pattern at the start and towards the end indicating that they are stable for the current computations. The burst in growth for frequencies is earliest for $n=16$ followed by $n=15$ ($f=426.60$ kHz), $n=14$ ($f=398.16$ kHz), $n=13$ ($f=369.72$ kHz), $n=12$ ($f=341.28$ kHz) and $n=11$. Similar trend was observed for frequencies $n=7$ ($f=199.08$ kHz) to $n=11$ - higher frequencies reaching synchronization point first.

Next figures show one on one comparison of pressure perturbation amplitudes for ideal and real gas simulations for each frequency. For frequencies upto $n=7$ ($f=199.08$ kHz) (Fig. 27(a), Fig. 27(b), Fig. 26(c) and Fig. 26(d)) the initial growth is similar for the two cases. Towards the exit real gas simulations tend to show a burst of growth, but amplitudes for both cases remain close. For frequencies $n=8$ ($f=227.52$ kHz) and $n=9$ ($f=255.96$ kHz) (Fig. 26(e) and Fig. 26(f)), the amplitudes are very similar for ideal and real gas simulations for the region not showing the second mode growth. For real gas simulations the frequencies start exponential growth towards the end of the computational zone. Ideal gas amplitudes remain low for the computed zone. Note that $n=9$ for ideal gas simulations does not show a second mode growth when real gas simulations do and for $n=8$ it is not clear whether ideal gas simulations would grow or not. Since $n=11$ ($f=312.84$ kHz) is unstable for ideal gas at about this location and $n=10$ ($f=284.40$ kHz) and $n=9$ are stable, $n=8$ has to be stable at least until frequencies $n=9$ and $n=10$ show a second mode growth.

For frequency $n=10$ ($f=284.40$ kHz) (Fig. 27(g)), the growth of amplitudes is very similar for ideal and real gases for the computed domain except at the end where real gas simulations show a second mode instability (exponential growth) whereas ideal gas simulation remain second mode stable. Frequency $n=11$ ($f=312.84$ kHz) (Fig. 27(h)) is second mode unstable for both ideal gas and real gas simulations. Ideal gas runs showing a steeper amplitude increase than real gas indicating a higher growth rate for the frequency. Frequency $n=9$ ($f=255.96$ kHz) for real gas simulations is also plotted from comparison. $N=9$ is the most unstable frequency for real gas simulations and $n=11$ is most unstable for ideal gas simulations. The amplitudes for $n=9$ real gas and $n=11$ ideal gas show very similar amplitudes indicating similar growth rates. It can be concluded that real gas effects do not effect the growth rate of most unstable frequency.

For frequencies $n=12$ ($f=341.28$ kHz) to $n=16$ ($f=455.04$ kHz) (Fig. 27(i), Fig. 27(j), Fig. 27(k), Fig. 27(l) and Fig. 27(m)), the amplitudes predicted by ideal gas simulations show a larger magnitude as compared to real gas predictions. For $n=13$ ($f=369.72$ kHz) perturbation amplitudes for ideal gas predictions seem to grow very rapidly but phase velocity plots do not show the presence of synchronization point. So it is likely that this is not second mode instability and would decay further downstream. For frequencies $n=14$ ($f=398.16$ kHz) to $n=16$, though amplitudes predicted by ideal gas simulations are larger, both ideal gas and real gas predict the decay of disturbance amplitudes indicating that these disturbances did not excite second modes in the boundary layer.

As discussed earlier, second mode instability is the result of synchronization of Mode I with second mode (Mack modes). The phase velocity diagrams show this point as the intersection of phase velocities for Mode I family of curves with Mach modes. Figure 28 shows phase velocities as function of natural coordinates for real gas simulations. For the computed zone, frequencies $n=1$ ($f=28.44$ kHz), $n=2$ ($f=56.88$ kHz) and $n=3$ ($f=85.32$ kHz) start off at a phase velocity of about 1.15 and remain at that value (Fig. 28(a)). The trend is similar for $n=3$ (Fig. 28(b)), but for $n=4$ ($f=113.76$ kHz), $n=5$ ($f=142.2$ kHz) and $n=6$ ($f=170.64$ kHz) the phase velocity decreases rapidly. However none of the curves reach velocity low enough for the disturbance to be in synchronization with the Mack modes. It is expected that synchronization point for these frequencies is further downstream. Frequencies $n=7$ ($f=199.08$ kHz), $n=8$ ($f=227.52$ kHz), $n=9$ ($f=255.96$ kHz), $n=10$ ($f=284.40$ kHz) and $n=11$ ($f=312.84$ kHz) (Fig. 27(c) and Fig. 27(d)) show a decrease in phase velocity from 1.15 to about 0.8 indicating a possibility of synchronization with Mach modes. The exponential growth for these frequencies shows that they have indeed excited the second mode instability. Frequencies $n=12$ ($f=341.28$ kHz), $n=13$ ($f=369.72$ kHz), $n=14$ ($f=398.16$ kHz), $n=15$ ($f=426.60$ kHz) and $n=16$ ($f=455.04$ kHz)

(Fig. 27(e) and Fig. 27(f)) do now show a decrease in phase velocities indicating that they have not reached synchronization point yet. Since these are higher frequencies they are not expected to reach synchronization point after lower frequencies and hence are stable for current computations.

Figure 29 shows phase velocities as a function of natural coordinates for ideal gas simulations. Frequencies $n=1$ ($f=28.44$ kHz) to $n=6$ ($f=170.64$ kHz) (Fig. 29(a)) do not show any decrease in phase velocity for the current domain. Frequency $n=7$ ($f=199.08$ kHz) (Fig. 29(b)) decreases towards the exit but it is not certain whether it will decrease or increase further downstream. Since frequencies $n=8$ ($f=227.52$ kHz) (Fig. 29(b)), $n=9$ ($f=255.96$ kHz) and $n=10$ ($f=284.40$ kHz) (Fig. 28(c)) do not show any decrease in phase velocities it is probable that $n=7$ would also not show any decrease and hence will not show second mode growth. It is also possible that $n=7$ is the third mode instability and phase velocity decreases further downstream and amplitudes for this frequency show exponential growth. For frequency $n=11$ ($f=312.84$ kHz) (Fig. 28(d)), phase velocity falls to about 0.8 at the end of the domain. The amplitude for pressure perturbation for this frequency also shows a exponential growth indicating a second mode instability. However for frequencies $n=12$ ($f=341.28$ kHz) to $n=16$ ($f=455.04$ kHz) (Fig. 28(e) and Fig. 28(f)) the phase velocity does not decrease and it expected that these frequencies will not excite unstable Mack modes. As a rule of thumb, higher frequencies become unstable earlier than lower frequencies (due to growing boundary layer the frequency for unstable mode decreases).

3. Comparison with Related Work

There have been limited studies on hypersonic transitory flows with real gas effects. Thermochemical nonequilibrium has only been recently included in theoretical studies via LST.^{5,6} Numerical studies on receptivity and transitory flows with real gas effects have recently begun with the development of numerical codes capable of simulating flow fields with thermochemical nonequilibrium. Study of transition via LST with real gas effects include efforts by Malik et al.,⁷ Stuckert and Reed,¹⁶ Johnson et al.,¹⁷ MacLean et al.⁴⁷ and Hudson et al.⁶ Numerical simulation of transitory flows include research efforts by Ma and Zhong,¹⁸ Stemmer et al.,⁴⁸ and Parsons.⁴⁹ The studies are not conclusive. A more comprehensive study on effects of real gas on laminar turbulent transition is needed. The following paragraphs will compare current results with results obtained by some of the above mentioned researchers.

Stemmer et al.⁴⁸ simulated unsteady flow over a flat plate and found that for real gas simulations the perturbations are not as prominent as the ideal gas runs. This is contrary to the findings of current study where nonequilibrium effects tend to destabilize the flow. However the reader must keep in mind that for the current case the real gas effects tend to increase the temperature of the flowfield - not usual for hypersonic test cases in literature. Also the current study is on a blunt cone with Stemmer et al.⁴⁸ simulated flow over a flat plate.

Earlier computations by Malik⁷ found real gas effects to increase the growth rate (cooling effect) and lower the unstable frequencies (heating effect) for second mode instability. His case was a Mach 10 air flow over a flat plate. Current simulations show similar growth rates for ideal and real gas simulations. If unstable frequencies are averaged, the current computations predict lower unstable frequencies for real gas simulations in comparison to ideal gas simulations. In addition, real gas effect tend to broaden the frequency range for instability (real gas simulations were unstable over a larger range of frequencies).

Johnson et al.¹⁷ found that for lower frequencies reactions tend to destabilize the flow while for higher frequencies reactions stabilize the flow. In current simulations, for lower frequencies (Fig. 27(b) and 26(c)) ideal gas simulations show smaller amplitudes as compared to real gas simulations indicating destabilizing nature of thermochemical effects. But for higher frequencies (Fig. 27(i), Fig. 27(j) and Fig. 27(k)) ideal gas show higher growth indicating stabilizing effect of thermochemical phenomenon. Johnson et al.¹⁷ also simulated cases where heat of reactions were reversed. This is as if instead of reducing the temperature, the chemical reactions would increase the temperatures. This is similar to the current computations where the temperature increases due to recombination reactions. The effect destabilized the flow. For current simulations, a larger range of frequencies were found unstable for real gas simulations as compared to ideal gas simulations.

Hudson et al.⁶ simulated Mach 10 and Mach 15 flow and compared different wall boundary conditions, effects of chemical equilibrium, nonequilibrium, thermochemical nonequilibrium and perfect gas simulation for instability predictions. They found that in upstream region chemical equilibrium effects were most destabilizing while in downstream region chemical nonequilibrium effects were most destabilizing. Thermochemical nonequilibrium effects were found to stabilize the flow always. This is contrary to current results. Current

simulations predict a wider range of unstable frequencies for real gas simulations as compared to ideal gas simulations, although the growth rate was predicted to be similar for real and ideal gas simulations. Hudson et al.⁶ found that in case of thermochemical nonequilibrium the boundary layer was thicker and hence most amplified frequency was higher. For current simulations the instability was observed far downstream of the nose region. Thermochemical nonequilibrium effects are prominent near the nose region. Current simulations predict identical boundary layer thickness for real and ideal gas simulation for most of the flow field. However, contrary to Hudson et al.,⁶ current simulations predict a lower most amplified frequency for real gas simulations.

Parsons et al.⁴⁹ earlier attempted to simulate unsteady flow over blunt 7° cone for the same free stream conditions as those for Mach 15.3 case by Lobb⁴⁴ using the algorithm developed by Prakash et al.¹⁵ The simulations predicted stable flow for their flow conditions and computational domain.

IX. Conclusion

Second mode instability was predicted for real gas simulations for a range of frequencies (n=7 f=199.08 kHz to n=11 f=312.84 kHz). Solution procedure involved extracting information for various modes using FFT. Ideal gas simulations were compared with real gas simulations. Ideal gas simulations predicted n=11 (312.84 kHz) as the only frequency showing second mode instability. Real gas simulations predicted a broader range of frequencies showing second mode instability. For this test case it was found that synchronization point for second mode is far downstream of the nose region where real gas effects are not strong. This is one of the first studies on receptivity of hypersonic boundary layer to free stream disturbances for flow over a blunt nose using shock fitting method.

Current computations predict similar behaviour to some of the results published in literature. Unlike Malik,⁷ current simulations showed similar growth rates for real gas case and like Malik⁷ lower unstable frequencies for real gas simulations. Results are very similar to predictions of Johnson et al.¹⁷ Real gas effects are destabilizing for lower frequencies and stabilizing for higher frequencies. Also, as predicted by Johnson et al.,¹⁷ heating effects due to chemical reactions destabilize the flow. Hudson et al.⁶ found a thicker boundary layer and hence higher most amplified frequency due to real gas effects. Current simulations predict identical boundary layer thickness in the unstable zone, and predict lower most unstable frequency for real gas simulations. Comparison with published data is not conclusive and further research is required to understand effects of thermochemical phenomenon. Overall, it was found in this study that real gas effects tend to destabilize the boundary layer flow. Real gas effects widened the spectrum of unstable frequencies and reduced the frequencies for which boundary layer is second mode unstable.

References

- ¹Bertin, J. and Cummins, R., "Critical Hypersonic Aerothermodynamic Phenomenon," *Annual Review of Fluid Mechanics*, Vol. 38, 2006, pp. 129–57.
- ²Reshotko, E., "Transition Issues for Atmospheric Entry," *Journal of Spacecraft and Rockets*, Vol. 45, 2008, pp. 161–164.
- ³Mack, L., "Boundary Layer Stability Theory," Tech. Rep. JPL Report 900-277 Rev A, Jet Propulsion Laboratory, Pasadena, CA, 1969.
- ⁴Fedorov, A., "Transition and Stability of High-Speed Boundary Layers," *Annual Review of Fluid Mechanics*, Vol. 49, 2011, pp. 79–95.
- ⁵Mack, L., "Boundary layer linear stability theory," AGARD Report, 1984.
- ⁶Hudson, L., Chokani, N., and Candler, G., "Linear Stability in Hypersonic Flow in Thermochemical Nonequilibrium," *AIAA Journal*, Vol. 53, No. 1, 1997.
- ⁷Malik, M. and Anderson, E., "Real Gas Effects on Hypersonic Boundary-Layer Stability," *Physics of Fluids A*, Vol. 3, No. 5, 1991.
- ⁸Wadhams, T. and Holden, M., "Summary Of Experimental Studies For Code Validation in the LENS Facility and Comparisons with Recent Navier-Stokes and DSMC Solutions for Two-and Three-Dimensional Separated Regions in Hypervelocity Flows," *AIAA Conference*, No. AIAA 2004-917, 2004.
- ⁹Cheatwood, F. and Gnoffo, P., "Users Manual for the Langley Aerothermal Upwind Relaxation Algorithm (LAURA)," Tech. rep., NASA, 1996.
- ¹⁰Gnoffo, P., Gupta, R., and Shinn, J., "Conservation Equations and Physical Models for Hypersonic Air Flows in Thermal and Chemical Nonequilibrium," Tech. Rep. NASA TP-2867, NASA, 1989.
- ¹¹Wright, M., Candler, G., and Bose, D., "Data-Parallel Line Relaxation Method for the Navier-Stokes Equations," *AIAA Journal*, Vol. 36, No. 9, 1998.
- ¹²Nompelis, I., Drayna, T., and Candler, G., "Development of a Hybrid Unstructured Implicit Solver for the Simulation of Reacting Flow over Complex Geometries," *AIAA Conference*, No. AIAA-2004-2227, 2004.

- ¹³Hash, D., Olejniczak, J., Wright, M., Dinish, P., Pulsonetti, M., Hollis, B., Gnoffo, P., Barnhard, M., Nompelis, I., and Candler, G., "FIRE II Calculations for Hypersonic Nonequilibrium Aerothermodynamics Code Validation: DPLR, LAURA and US3D," *AIAA Conference*, No. AIAA-2007-0605, 2007.
- ¹⁴Lewis, J. and Williams, I., "Flight Parameters and Vehicle Performance for Project FIRE Flight II, Launched May 22, 1965," Tech. Rep. NASA TN D-3569, NASA, 1966.
- ¹⁵Prakash, A., Parsons, N., Wang, X., and Zhong, X., "High-Order Shock-Fitting Methods for Hypersonic Flow with Chemical and Thermal Nonequilibrium," *AIAA Conference*, No. AIAA-2010-4997, 2010.
- ¹⁶Stuckert, G. and Reed, H., "Linear Disturbance in Hypersonic, Chemically Reacting Shock Layers," *AIAA Journal*, Vol. 32, No. 7, 1994.
- ¹⁷Johnson, H., Trevor, G., and Candler, G., "Numerical Study of Hypersonic Reacting Boundary Layer Transition on Cones," *Physics of Fluids*, Vol. 10, No. 10, 1998.
- ¹⁸Ma, Y. and Zhong, X., "Receptivity to Freestream Disturbances of a Mach 10 Nonequilibrium Reacting Oxygen Flow over a Flat Plate," *AIAA Conference*, No. AIAA-2004-0256, 2004.
- ¹⁹Stemmer, C. and Adams, N., "Investigation of Hypersonic Flat-Plate Boundary Layer Transition by Direct Numerical Simulation," *High Performance Computing in Science and Engineering '04*, Springer, 2005.
- ²⁰Lele, S., "Compact Finite-Difference Schemes with Spectral-Like Resolution," *Journal of Computational Physics*, Vol. 104, 1992, pp. 16–42.
- ²¹Park, C., *Nonequilibrium Hypersonic Aerothermodynamics*, John Wiley and Sons, 1990.
- ²²Leyva, I., Laurance, S., Beierholm, W., Hornung, H., Wagnild, R., and Candler, G., "Transition Delay in Hypervelocity Boundary Layers by means of CO₂ Acoustic Instability Interactions," *AIAA Conference*, No. AIAA-2009-1287, 2009.
- ²³Wadhams, T., MacLean, M., Holden, M., and Berry, S., "A Review of Transition Studies on Full-Scale Flight Vehicles at Duplicated Flight Conditions in LENS Tunnels and Comparisons with Prediction Methods and Flight Measurement," *AIAA Conference*, No. AIAA 2010-1246, 2010.
- ²⁴Schneider, S., "Hypersonic Laminar Turbulent Transition on Circular Cones and Scramjet Forebodies," *Progress in Aerospace Sciences*, Vol. 40, 2004, pp. 1–50.
- ²⁵Wright, R. and Zoby, E., "Flight Boundary Layer Transition Measurements on a Slender Cone at Mach 20," *AIAA Conference*, No. AIAA-77-719, 1977.
- ²⁶Stetson, K., Thompson, E., Donaldson, J., and Siler, L., "Laminar Boundary Layer Stability Experiments on a Cone at Mach 8 Part 1: Sharp Cone," *AIAA Conference*, No. AIAA-83-1761, 1983.
- ²⁷Stetson, K., Thompson, E., Donaldson, J., and Siler, L., "Laminar Boundary Layer Stability Experiments on a Cone at Mach 8 Part 2: Blunt Cone," *AIAA Conference*, No. AIAA-84-0006, 1984.
- ²⁸Sherman, M. and Nakamura, T., "Flight Test Measurements of Boundary-Layer Transition on a Non-ablating 22 deg cone," *Journal of Spacecraft*, Vol. 7, No. 2, 1970.
- ²⁹Hornung, H., "Non-equilibrium Dissociating Nitrogen Flow over Spheres and Circular Cylinders," *Journal of Fluid Mechanics*, Vol. 53, No. 1, 1972, pp. 149–176.
- ³⁰Wen, C. and Hornung, H., "Nonequilibrium Dissociating Flow over Spheres," *Journal of Fluid Mechanics*, Vol. 299, 1995, pp. 389.
- ³¹Candler, G., *The Computation of Weakly Ionized Hypersonic Flows in Thermo Chemical Nonrquilibrium*, Ph.D. thesis, Stanford University, 1988.
- ³²Hornung, H., "Hypersonic Real-Gas Effects on Transition," *IUTAM Symposium on One Hundred Years of Boundary Layer Research Solid Mechanics and its Applications*, Vol. 129, 2006, pp. 335–344.
- ³³Germain, P. and Hornung, H., "Transition on Slender Cone in Hypervelocity Flow," *Experiments in Fluids*, Vol. 22, 1997, pp. 183.
- ³⁴Lee, T. and Zhong, X., "Spurious Numerical Oscillations in Simulation of Supersonic Flows Using Shock-Capturing Schemes," *AIAA Journal*, Vol. 37, No. 3, 1999.
- ³⁵Zhong, X., "High Order Finite-Difference Schemes for Numerical Simulation of Hypersonic Boundary Layer Transition," *Journal of Computational Physics*, Vol. 144, 1998, pp. 662–709.
- ³⁶Ma, Y. and Zhong, X., "Receptivity of Supersonic Boundary Layer over a Flat Plate. Part 1. Wave Structures and Interactions," *Journal of Fluid Mechanics*, Vol. 488, 2003, pp. 31–78.
- ³⁷Ma, Y. and Zhong, X., "Receptivity of Supersonic Boundary Layer over a Flat Plate. Part 2. Receptivity to Free Stream Sound," *Journal of Fluid Mechanics*, Vol. 488, 2003, pp. 79–121.
- ³⁸Wang, X. and Zhong, X., "Receptivity of a Hypersonic Flat-Plat Boundary Layer to Three-Dimensional Surface Roughness," *Journal of Spacecraft and Rockets*, Vol. 45, No. 6, 2008.
- ³⁹Ma, Y. and Zhong, X., "Boundary Layer Receptivity of Mach 7.99 Flow over a Blunt Cone to Free Stream Acoustic Waves," *Journal of Fluid Mechanics*, Vol. 556, 2006, pp. 55–103.
- ⁴⁰Olejniczak, J., Candler, G., Wright, M., Leyva, I., and Hornung, H., "Experimental and Computational Study of High Enthalpy Double-Wedge Flows," *Journal of Thermophysics and Heat Transfer*, Vol. 13, No. 14, 1999.
- ⁴¹Blottner, F., "Prediction of Electron Density in the Boundary Layer on Entry Vehicles with Ablation," *The Entry Plasma Sheath and its Effects on Space Vehicle Electromagnetic Systems, Volume I*, No. 13, 1970.
- ⁴²Park, C., "On Convergence of Computation of Chemically Reacting Flows," *AIAA Conference*, No. AIAA-85-0247, 1985.
- ⁴³Ma, Y. and Zhong, X., "Receptivity of Supersonic Boundary Layer over a Flat Plate. Part 3. Effects of different types of free-stream disturbances," *Journal of Fluid Mechanics*, Vol. 532, 2005, pp. 63–109.
- ⁴⁴Lobb, K., "Experimental Measurement of Shock Detachment Distance on Spheres Fired in Air at Hyper Velocities," *The High Temperature Aspects of Hypersonic Flow*, Pergamon Press, 1964.
- ⁴⁵Zhong, X., "Leading-edge Receptivity to Free-Stream Disturbance Waves for Hypersonic Flow Over a Parabola," *Journal of Fluid Mechanics*, Vol. 441, 2001, pp. 315–367.

⁴⁶Press, W., Teukolsky, S., Vetterling, W., and Flannery, B., *Numerical Recipes*, Cambridge University Press, 2001.

⁴⁷MacLean, M., Mundy, E., Wadhams, T., Holden, M., Johnson, H., and Candler, G., "Comparisons of Transition Prediction using PSE-Chem to Measurements for a Shock Tunnel Environment," *AIAA Conference*, No. AIAA-2007-4490, 2007.

⁴⁸Stemmer, C. and Adams, N., "Instabilities in Hypersonic Boundary Layer Under the Influence of High-temperature Gas Effects," *High Performance Computing in Science and Engineering '05*, Springer, 2006.

⁴⁹Parsons, N., Zhong, X., Kim, J., and Eldredge, J., "Numerical Study of Hypersonic Receptivity with Thermochemical Non-Equilibrium on a Blunt Cone," *AIAA Conference*, No. AIAA-2010-4446, 2010.

A. Figures

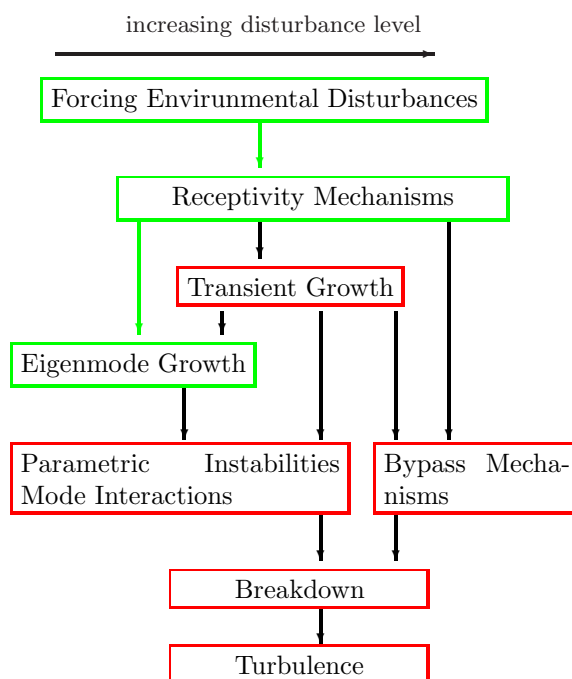


Figure 1. Paths to Turbulence.²

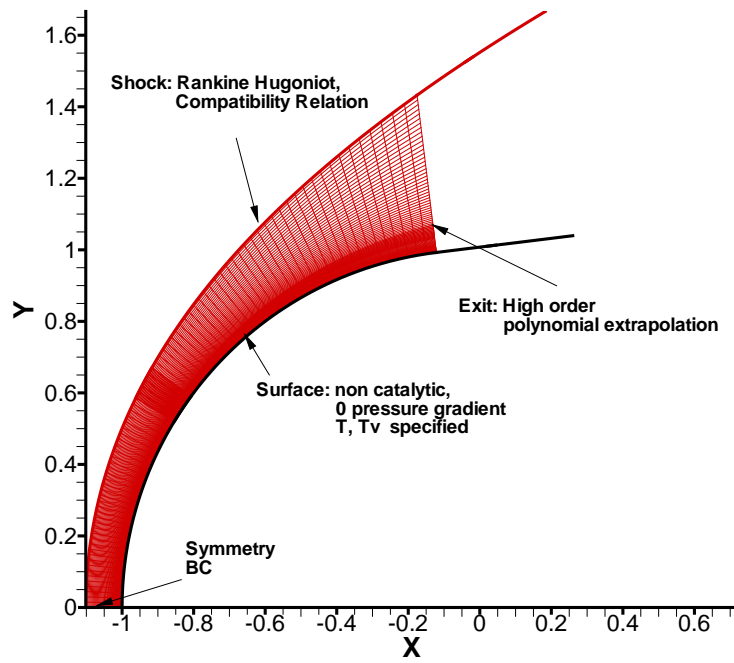


Figure 2. Boundary Conditions in the computational domain.

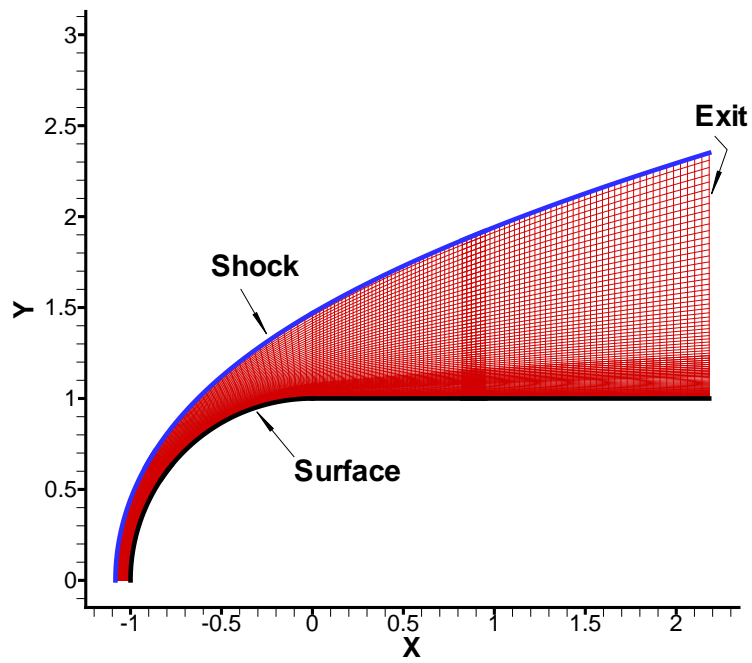


Figure 3. Computational domain.

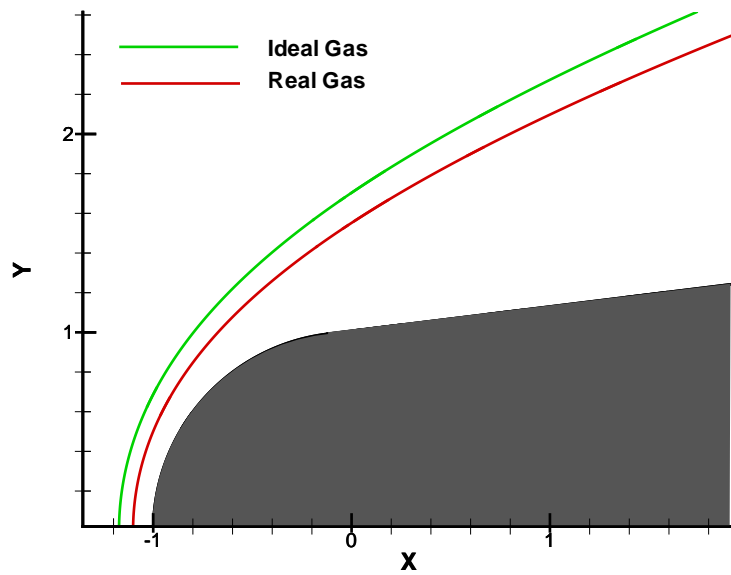


Figure 4. Shock standoff distance near spherical nose- green line: Ideal gas, red line: real gas simulations.

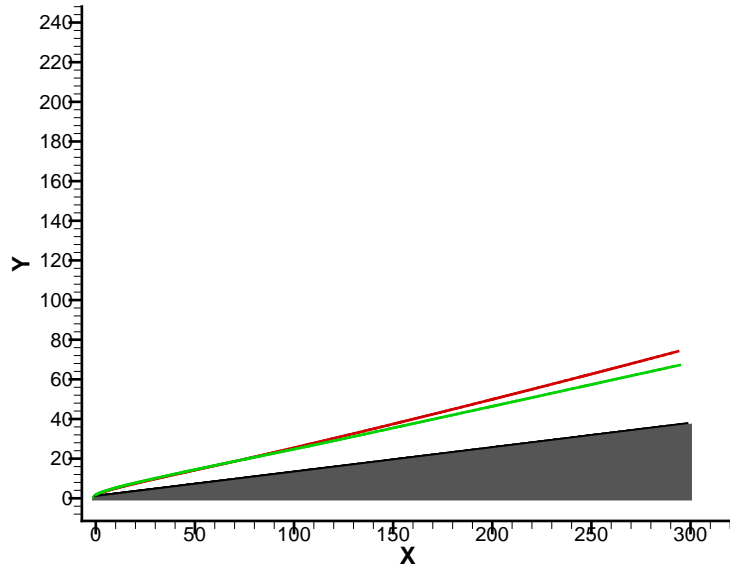


Figure 5. Shock standoff distance: green line: Ideal gas, red line: real gas simulations

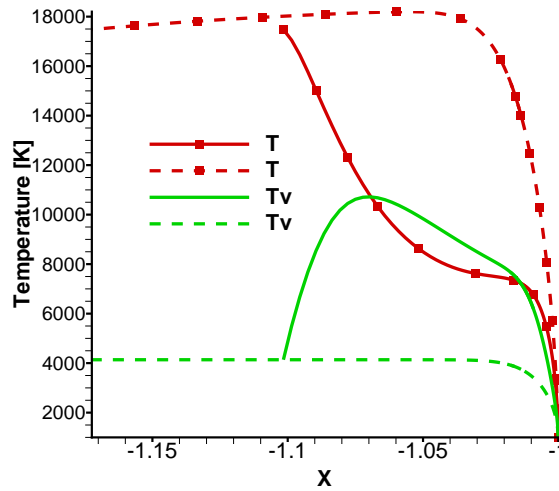


Figure 6. Temperatures along stagnation line. Dashed: Ideal gas; solid: real gas.

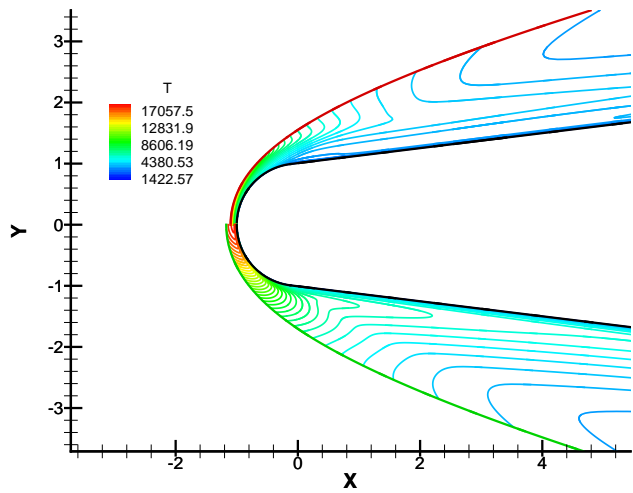


Figure 7. Temperature contours near stagnation region. Top: Real gas simulations; Bottom: Ideal gas simulations.

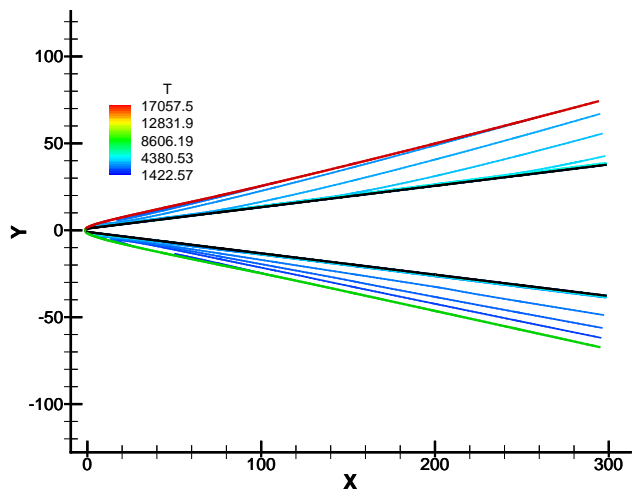


Figure 8. Temperature contours for flow field. Top: Real gas simulations; Bottom: Ideal gas simulations.

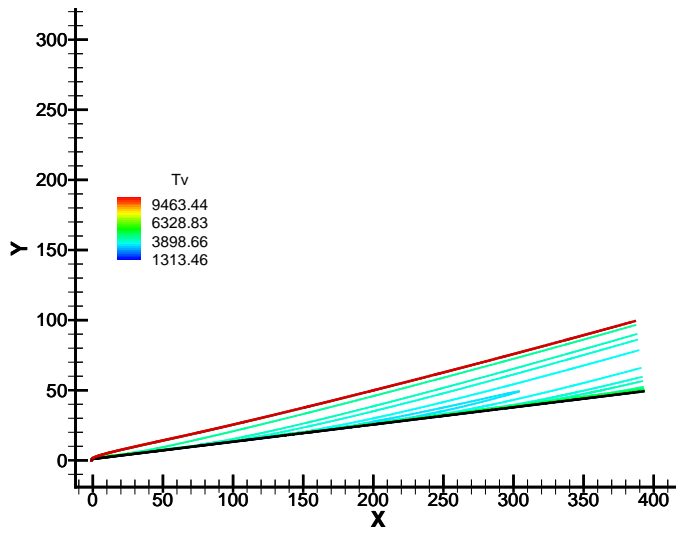
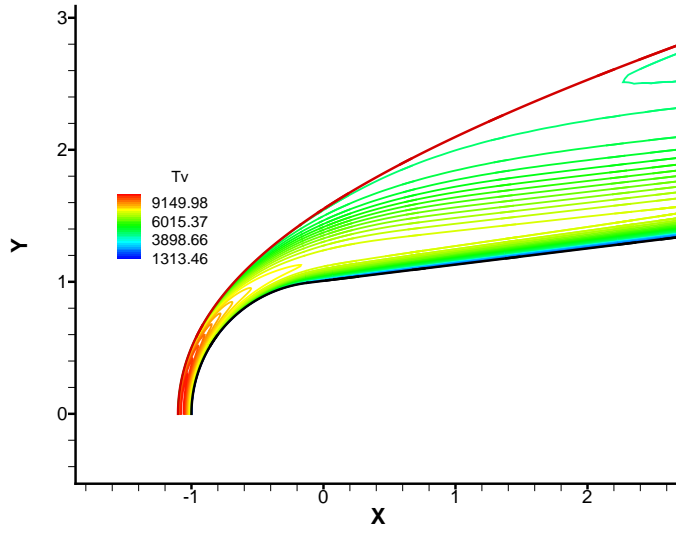


Figure 9. T_v contours for real gas simulations. Top: Stagnation region; Bottom: Flow field.

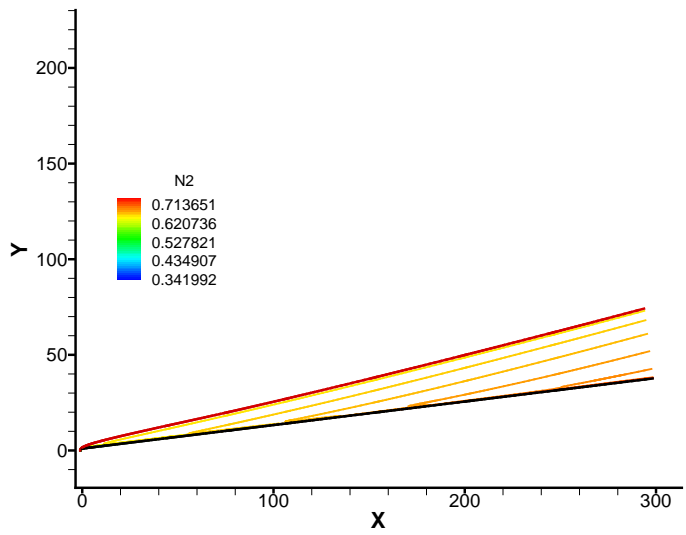
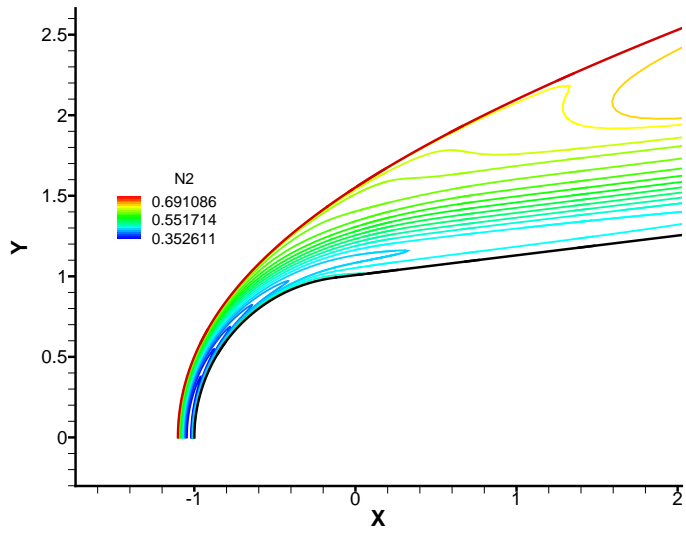
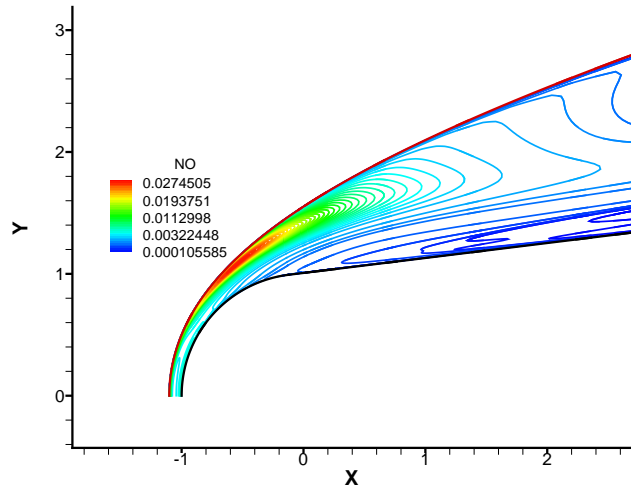
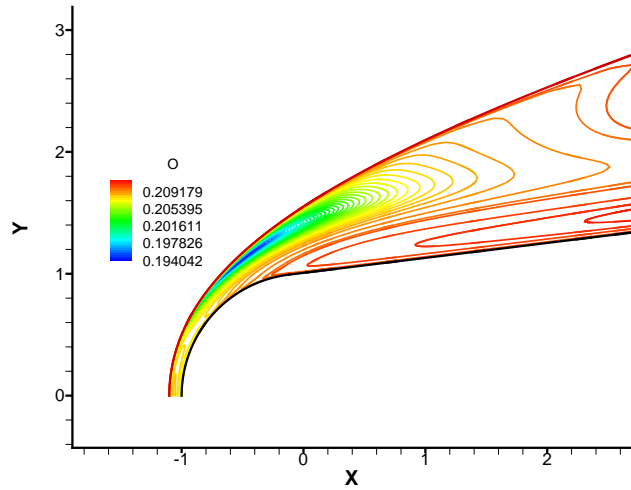


Figure 10. N_2 contours for real gas simulations. Top: Stagnation region; Bottom: Flow field.



(a) *NO* contours



(b) *O* contours

Figure 11. *NO* and *O* Contours for real gas simulations. Top: Stagnation region; Bottom: Flow field.

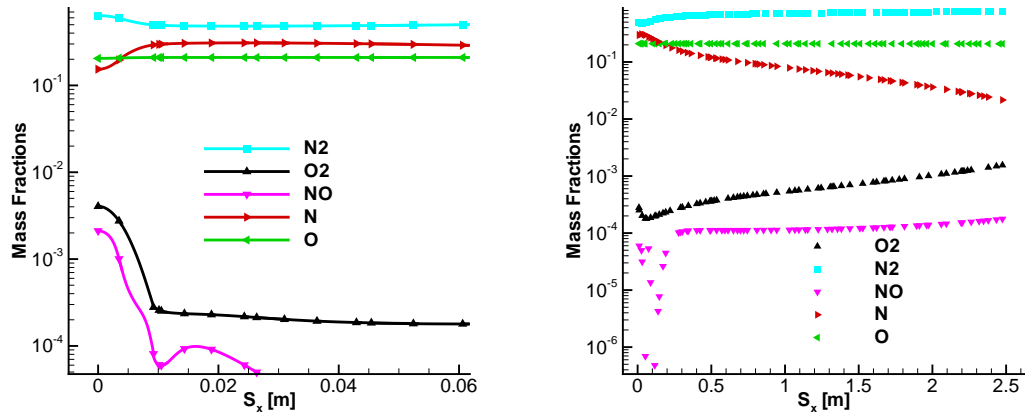


Figure 12. Mass fractions along surface of blunt cone. Left: Stagnation region; Right: Entire flow field.

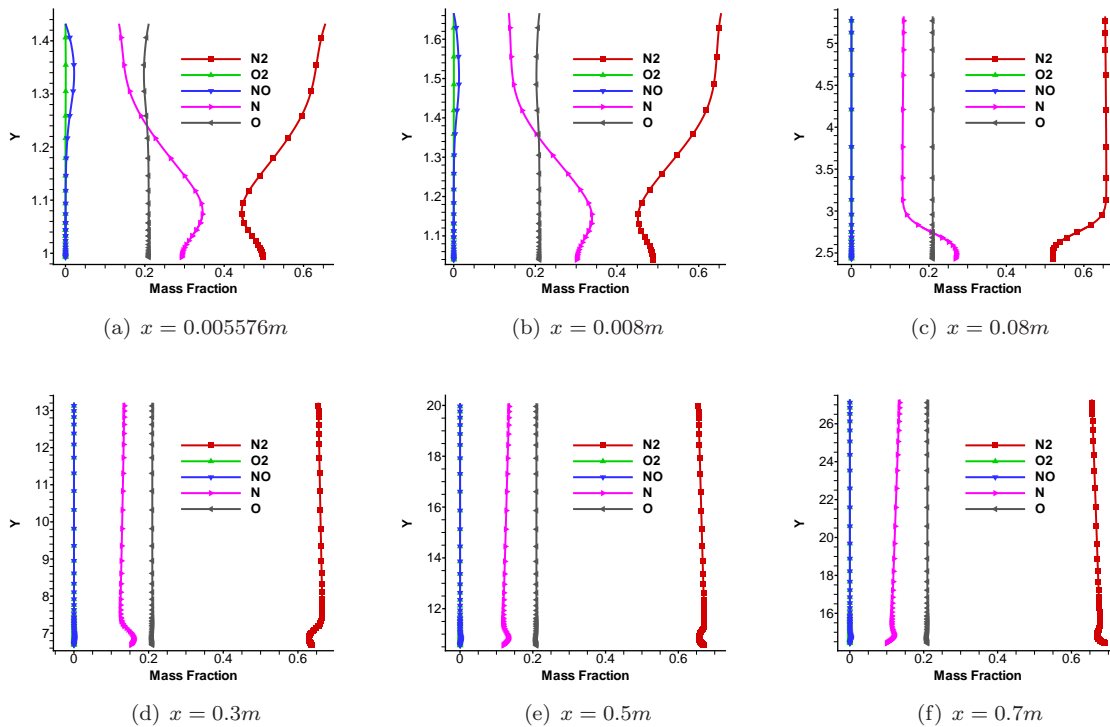


Figure 13. Boundary Layer profiles for Species mass fraction. Contd. next pg. ...

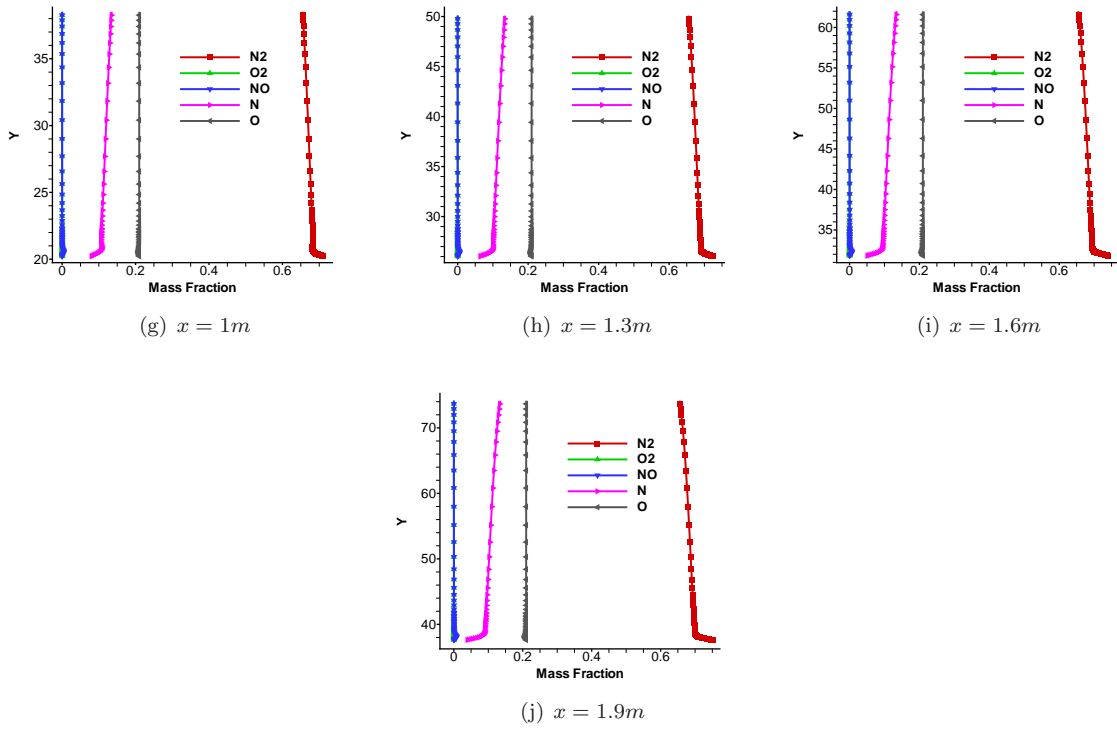


Figure 13. Boundary Layer profiles for species mass fraction.

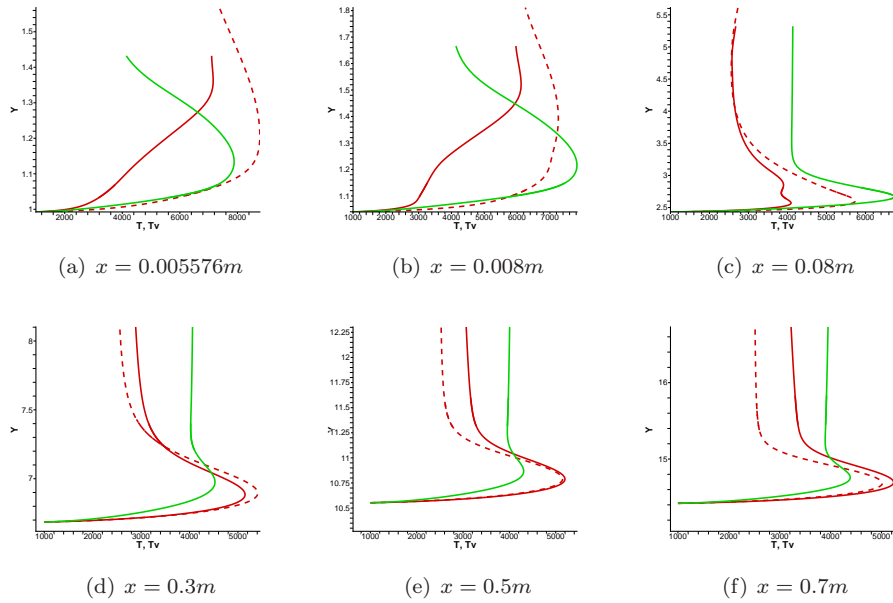


Figure 14. Boundary Layer profiles for Temperatures. Contd. next pg. ...

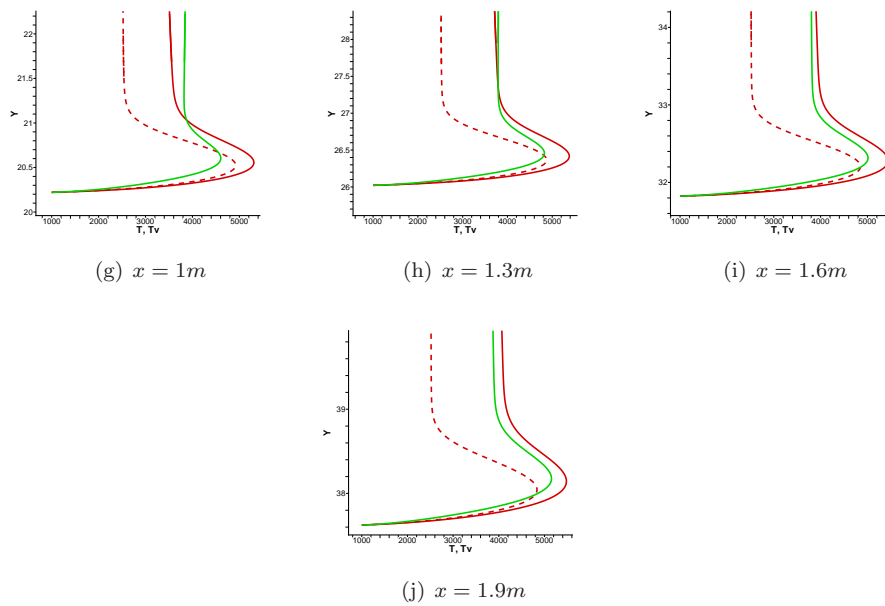


Figure 14. Boundary Layer profiles for Temperatures. Dashed lines are temperature from ideal gas simulations. Red line is translation-rotation temperature and green line is vibration temperature from real gas simulations.

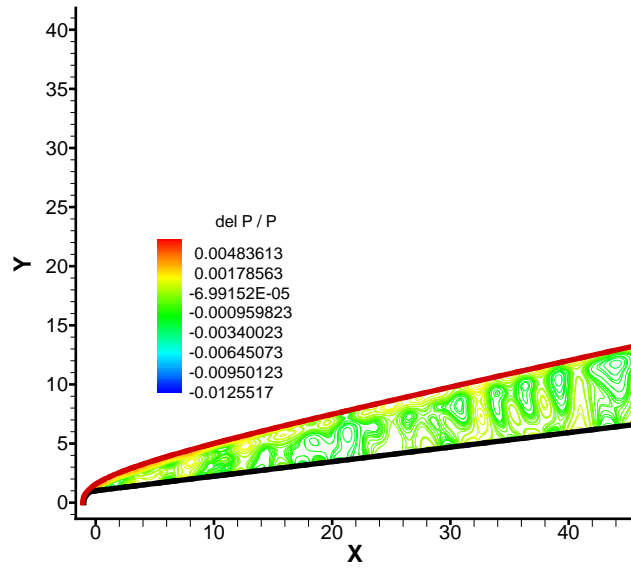


Figure 15. Contours of pressure disturbances using real gas Model 1.

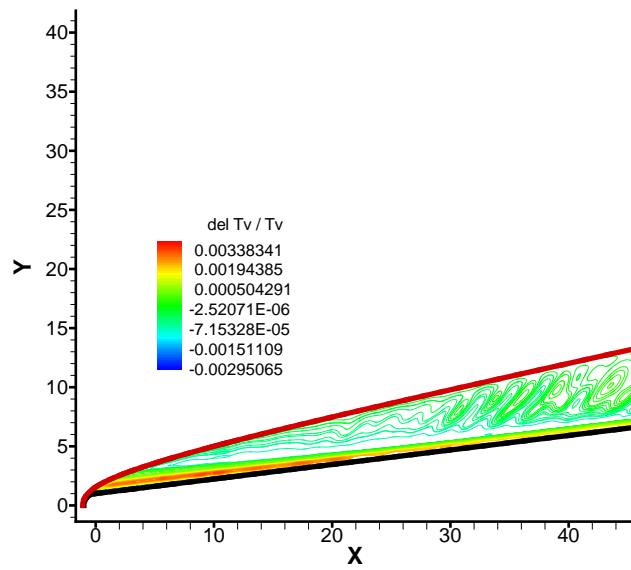


Figure 16. Contours of vibration temperature disturbances using real gas Model 1.

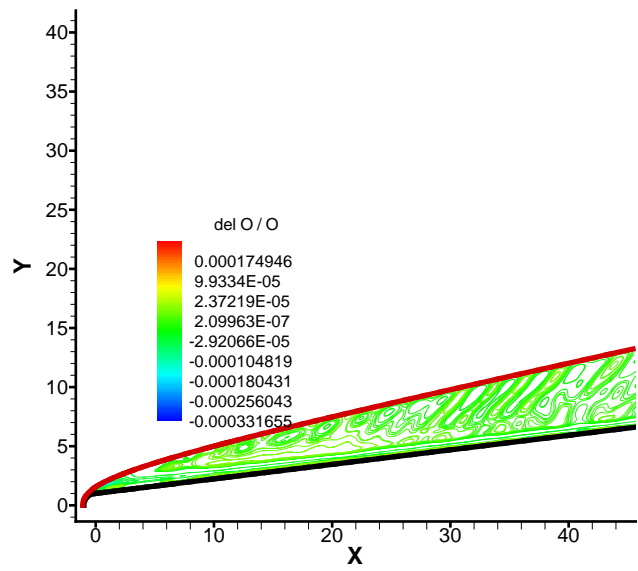
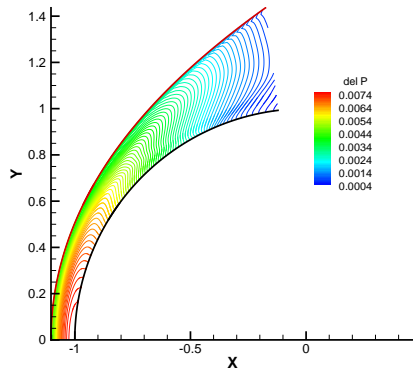
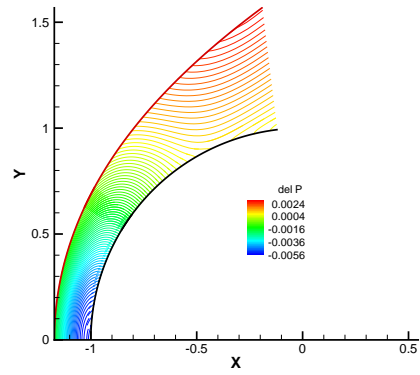


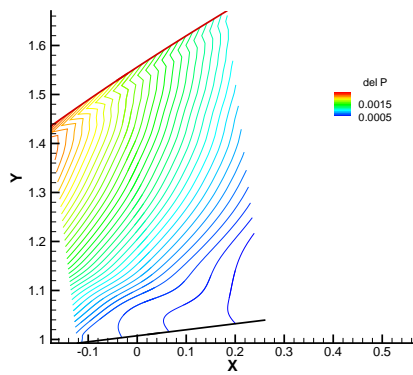
Figure 17. Contours of atomic oxygen mass fraction disturbances using real gas Model 1.



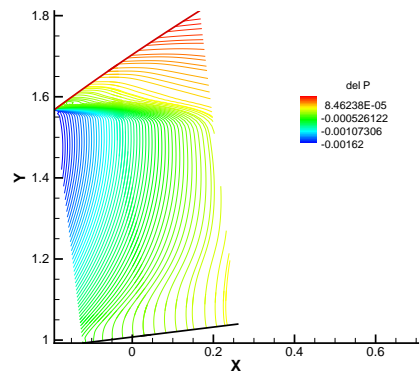
(a) zone 1 Real



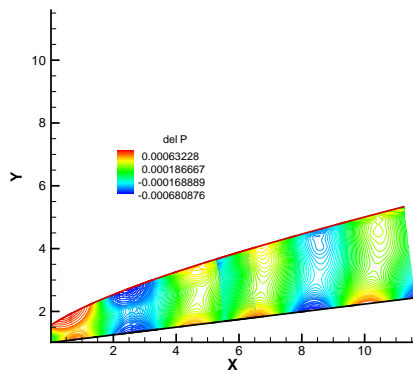
(b) zone 1 Ideal



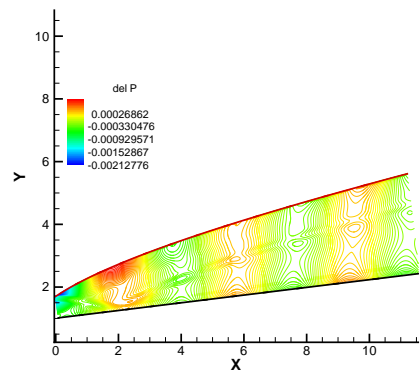
(c) zone 2 Real



(d) zone 2 Ideal

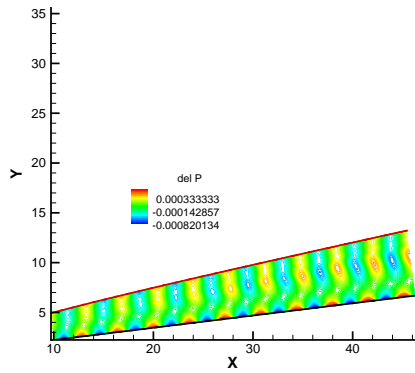


(e) zone 3 Real

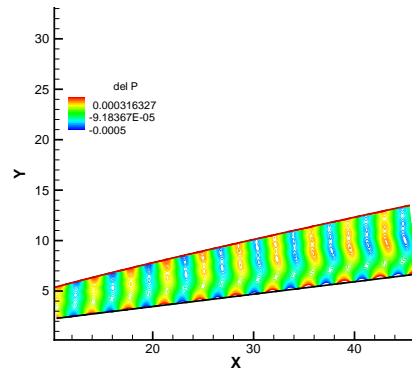


(f) zone 3 Ideal

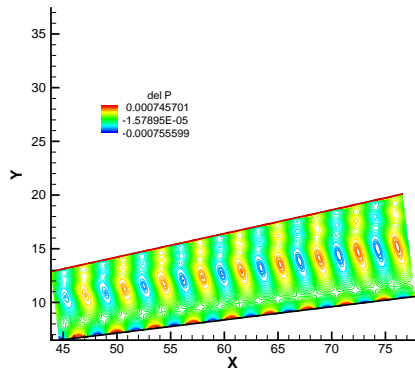
Figure 18. Unsteady contours for Pressure perturbations. Contd. next pg. ...



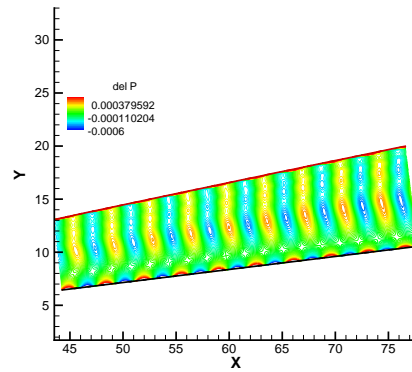
(g) zone 6 Real



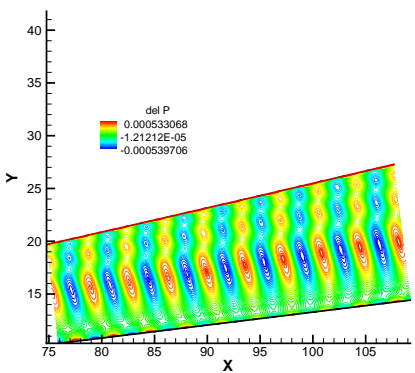
(h) zone 6 Ideal



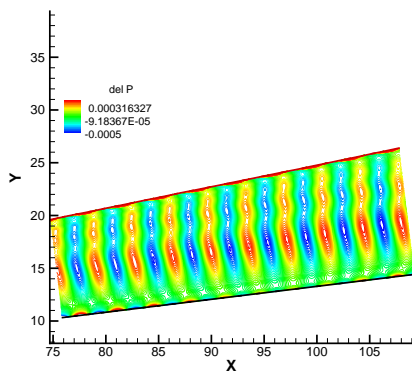
(i) zone 7 Real



(j) zone 7 Ideal

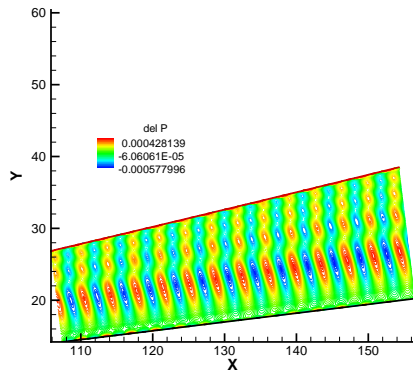


(k) zone 8 Real

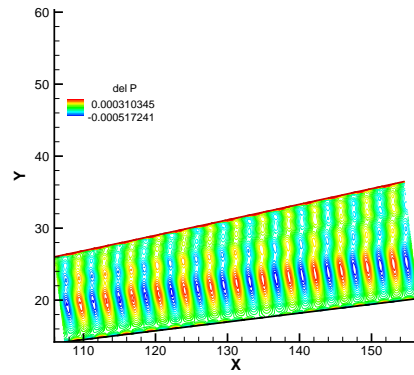


(l) zone 8 Ideal

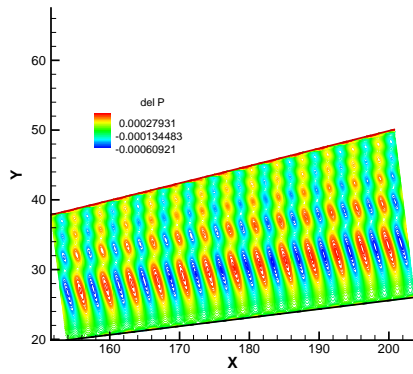
Figure 18. Unsteady contours for Pressure perturbations. Contd. next pg. ...



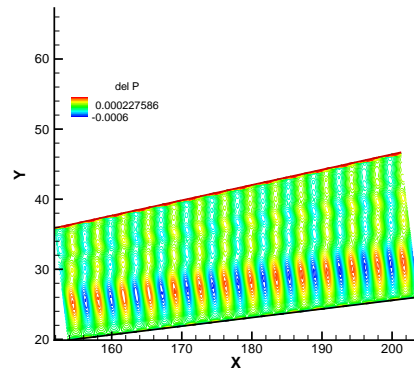
(m) zone 9 Real



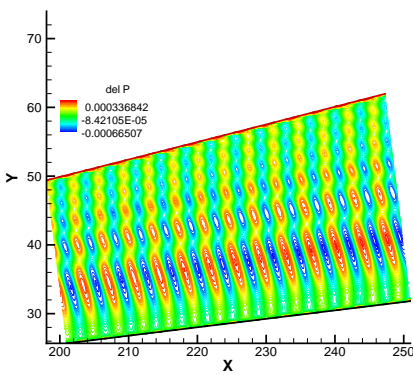
(n) zone 9 Ideal



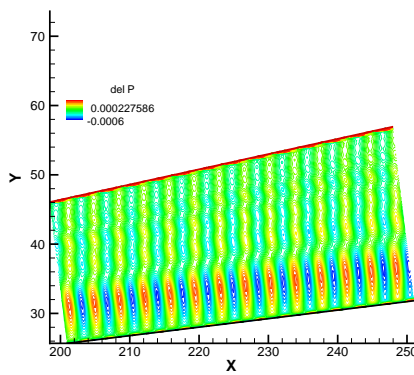
(o) zone 10 Real



(p) zone 10 Ideal

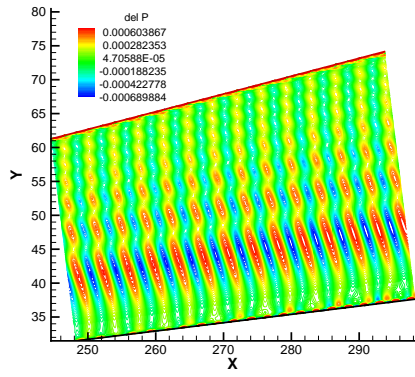


(q) zone 11 Real

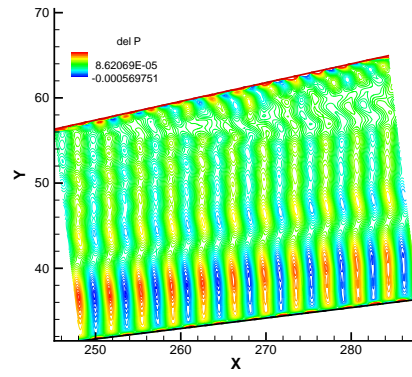


(r) zone 11 Ideal

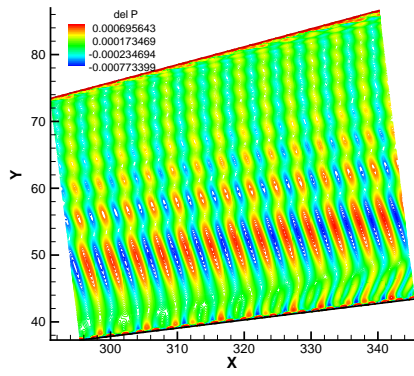
Figure 18. Unsteady contours for Pressure perturbations. Contd. next pg. ...



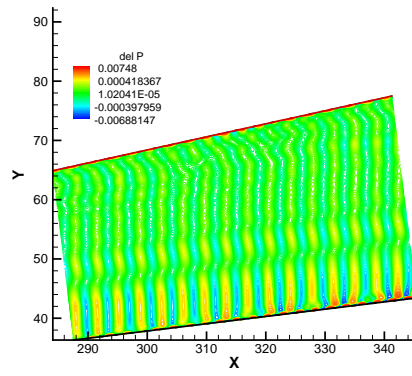
(s) zone 12 Real



(t) zone 12 Ideal

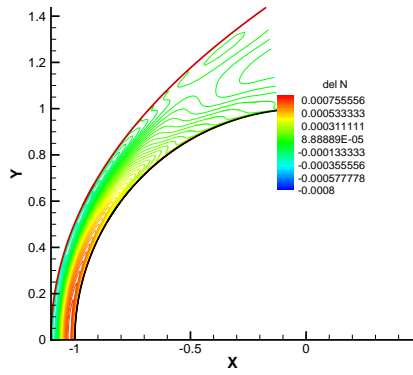


(u) zone 13 Real

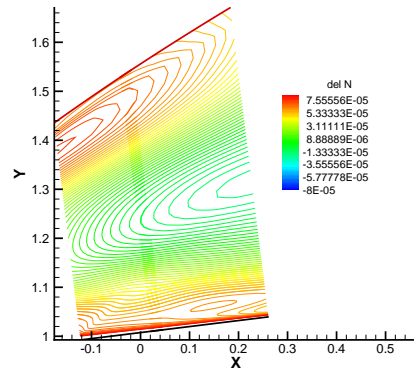


(v) zone 13 Ideal

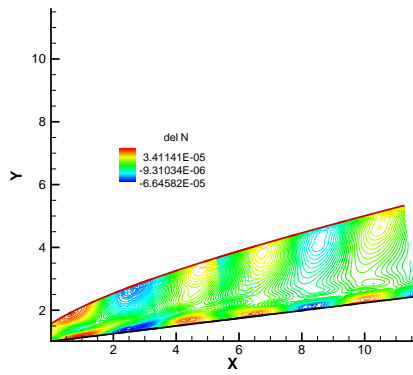
Figure 18. Unsteady contours for Pressure perturbations for frequency $n=11$ ($f=312.84$ kHz).



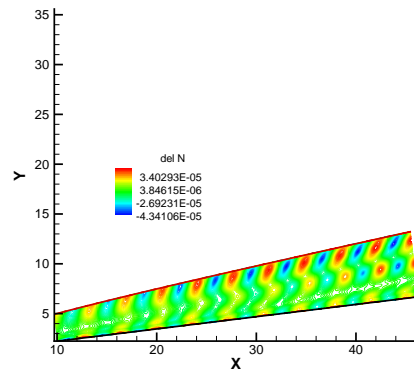
(a) zone 1



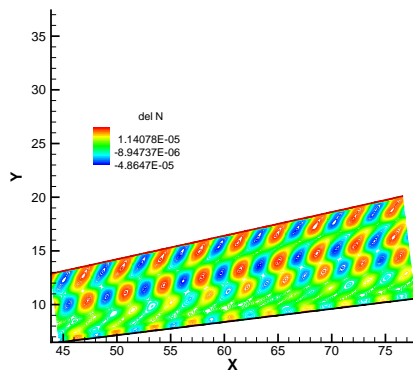
(b) zone 2



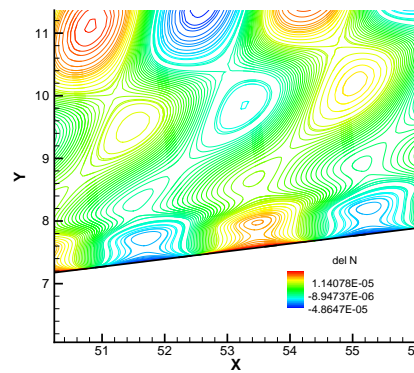
(c) zone 3



(d) zone 6

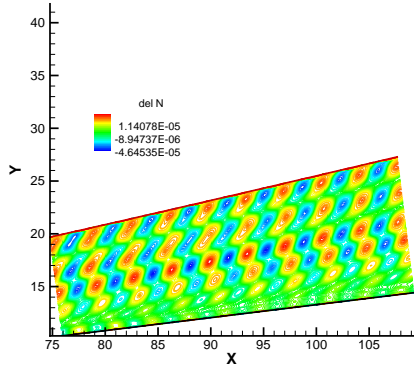


(e) zone 7

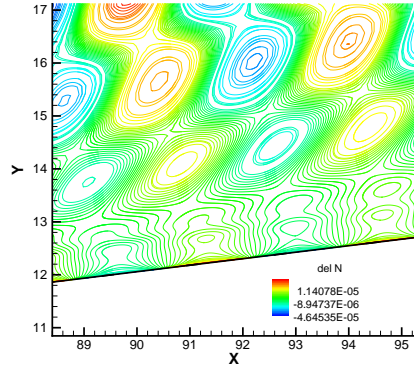


(f) zone 7, near surface

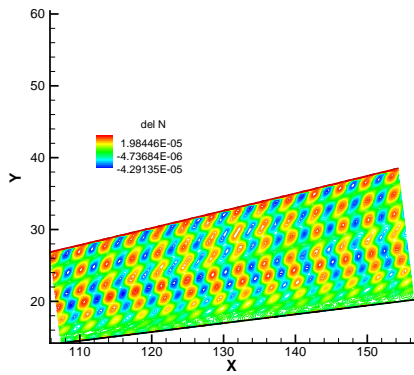
Figure 19. Unsteady contours for N mass fraction perturbations. Contd. next pg. ...



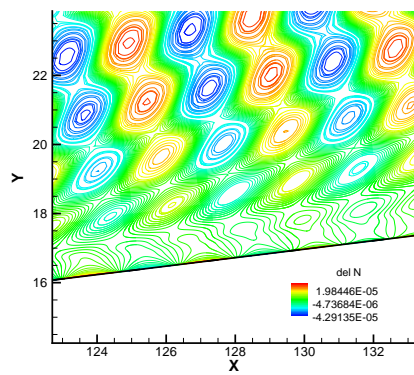
(g) zone 8



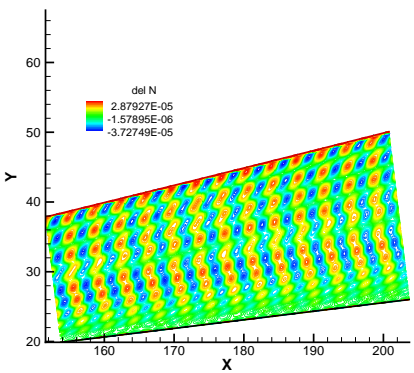
(h) zone 8, near surface



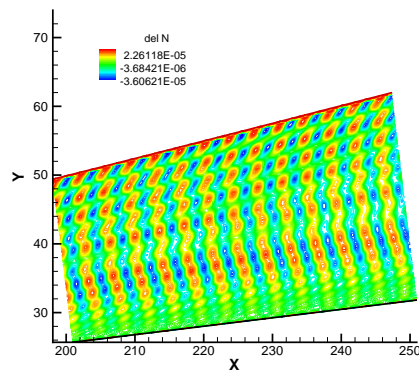
(i) zone 9



(j) zone 9, near surface

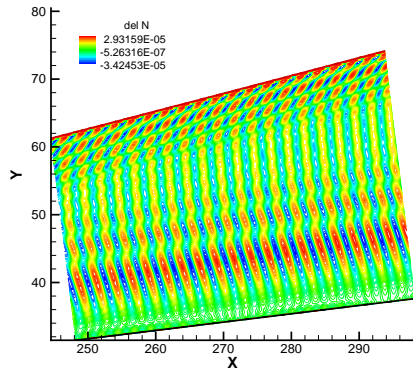


(k) zone 10

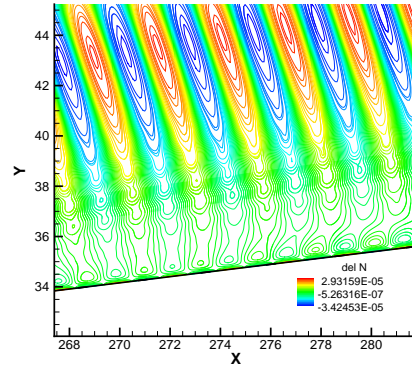


(l) zone 11

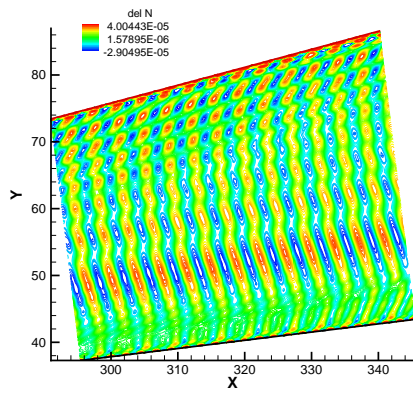
Figure 19. Unsteady contours for N mass fraction perturbations. Contd. next pg. ...



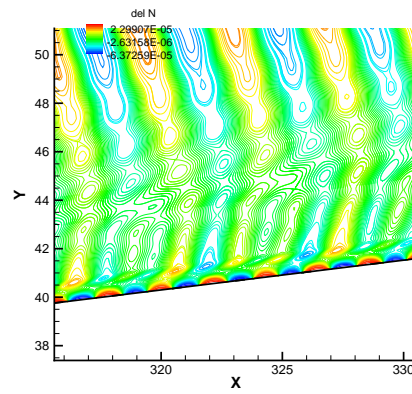
(m) zone 12



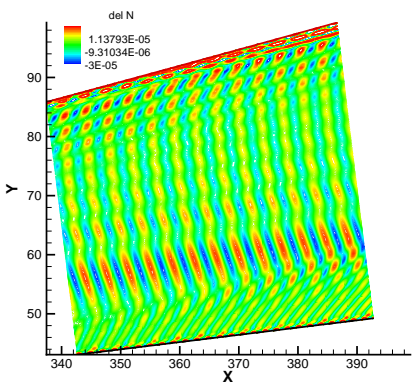
(n) zone 12, near surface



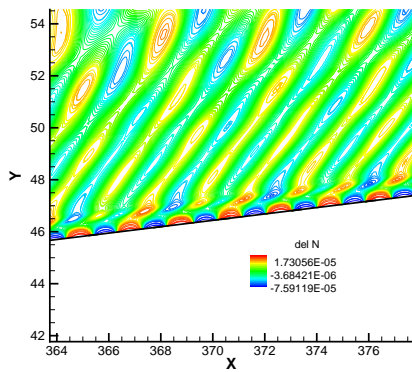
(o) zone 13



(p) zone 13, near surface



(q) zone 14



(r) zone 14, near surface

Figure 19. Unsteady contours for N mass fraction perturbations for frequency $n=11$ ($f=312.84$ kHz).

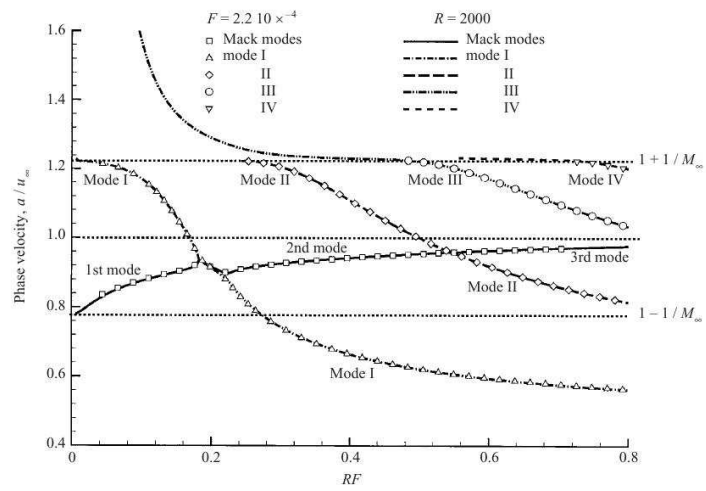


Figure 20. Phase velocity distributions for disturbance waves, Martin 2003.³⁶

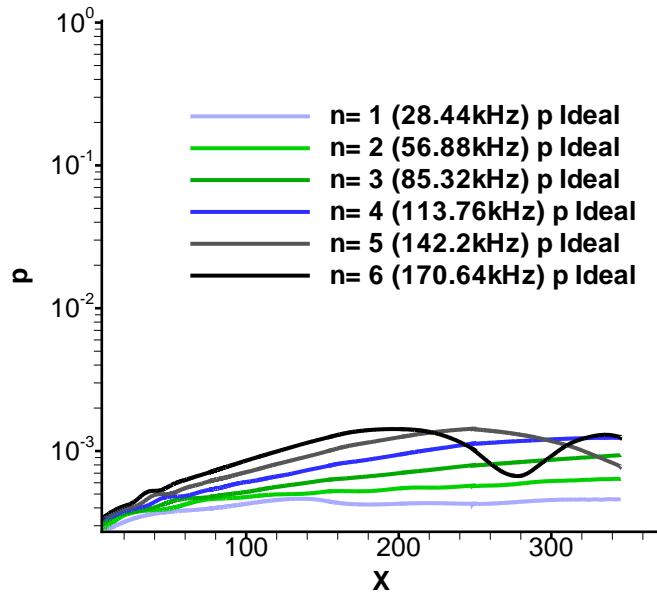


Figure 21. Amplitudes for pressure perturbations for ideal gas simulations, frequencies 1-6.

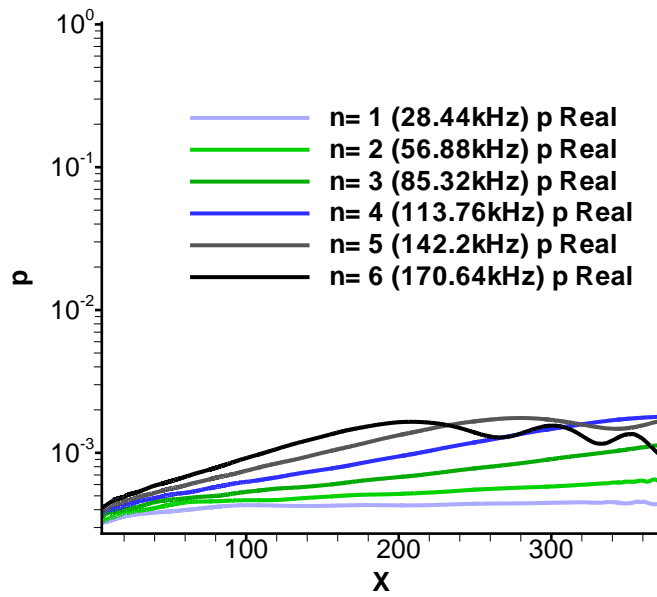


Figure 22. Amplitudes for pressure perturbations for real gas simulations, frequencies 1-6.

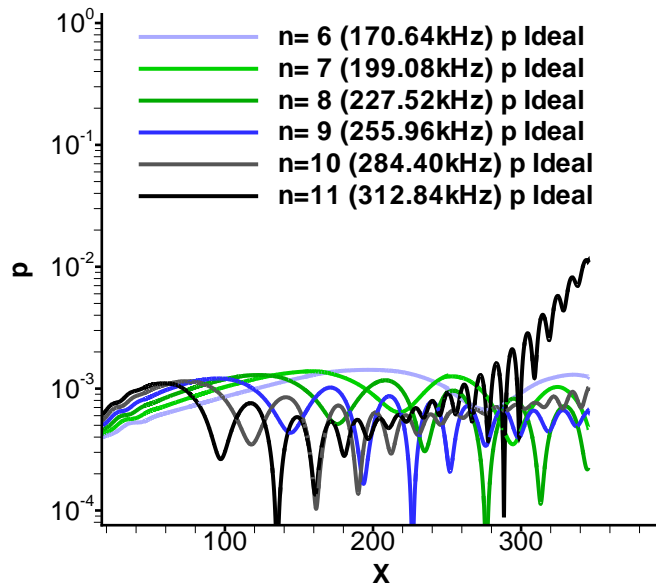


Figure 23. Amplitudes for pressure perturbations for ideal gas simulations, frequencies 6-10.

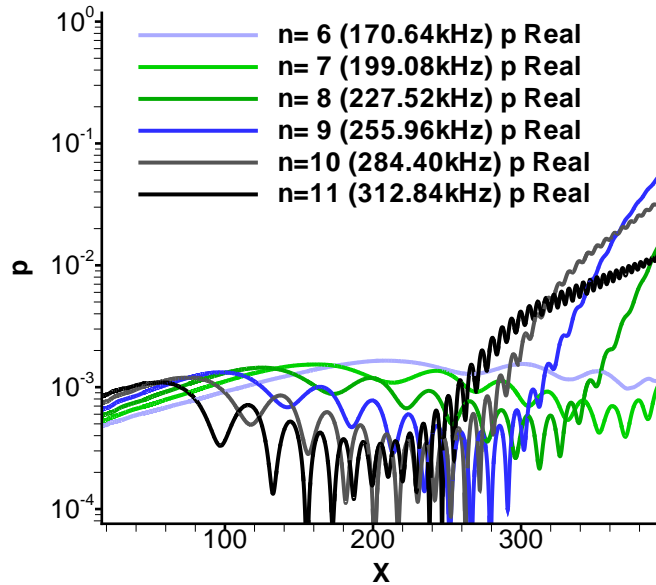


Figure 24. Amplitudes for pressure perturbations for real gas simulations, frequencies 6-10.

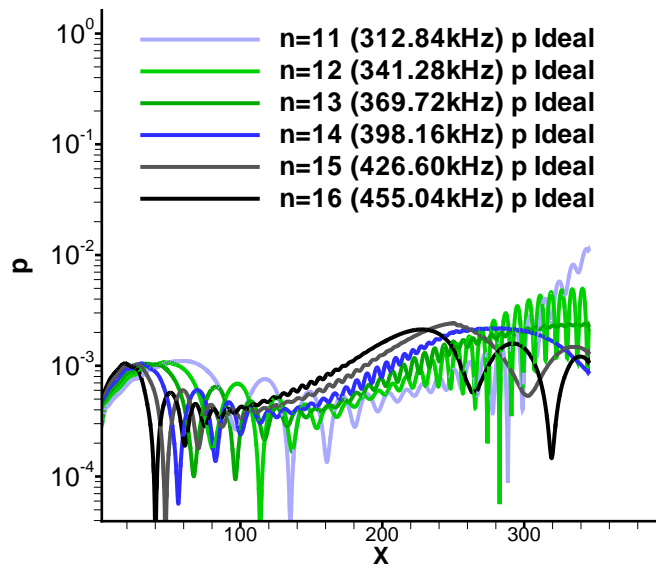


Figure 25. Amplitudes for pressure perturbations for ideal gas simulations, frequencies 11-16.

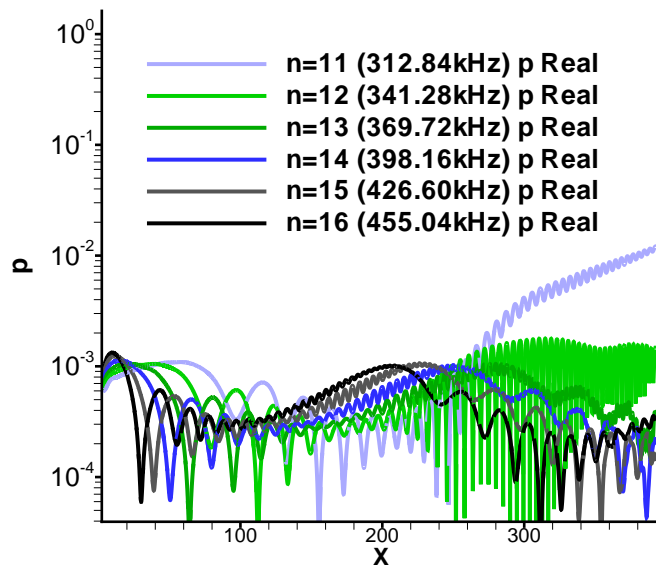
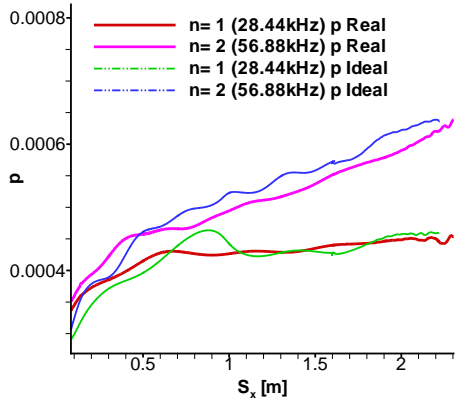
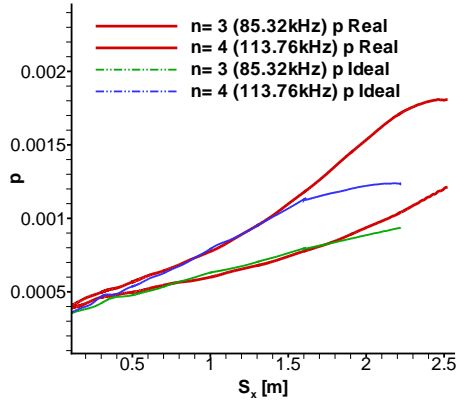


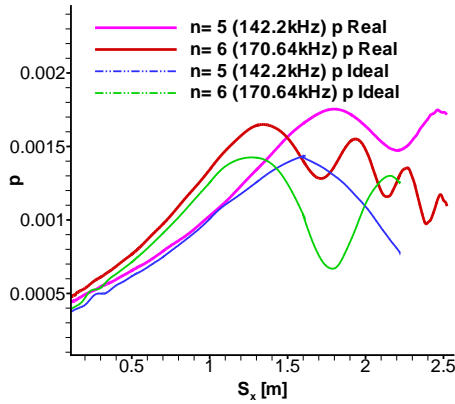
Figure 26. Amplitudes for pressure perturbations for real gas simulations, frequencies 11-16.



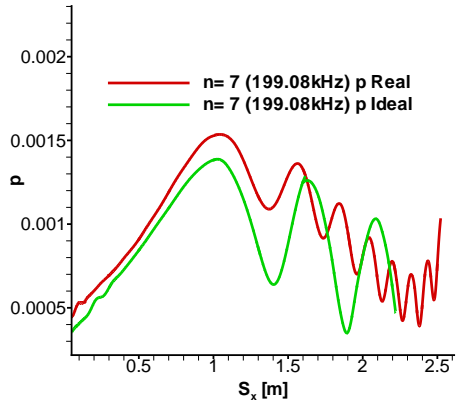
(a) $n=1,2$



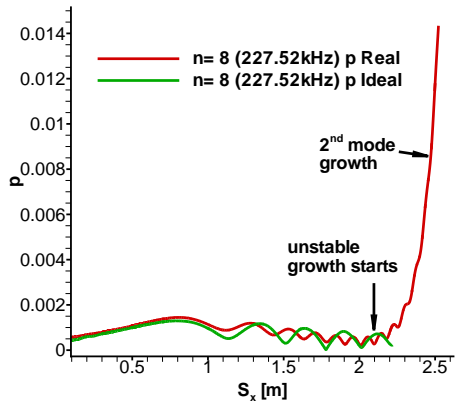
(b) $n=3,4$



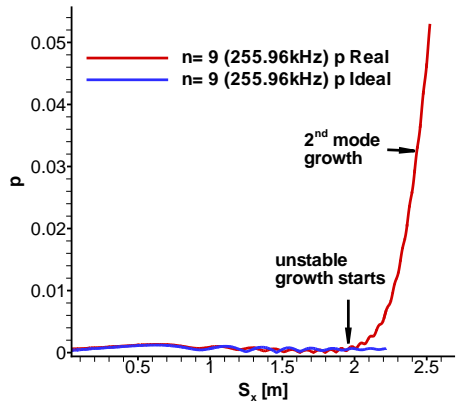
(c) $n=5,6$



(d) $n=7$

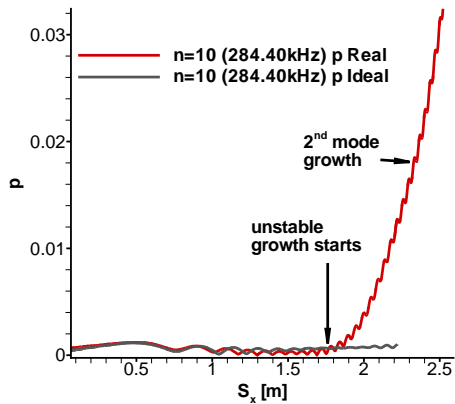


(e) $n=8$

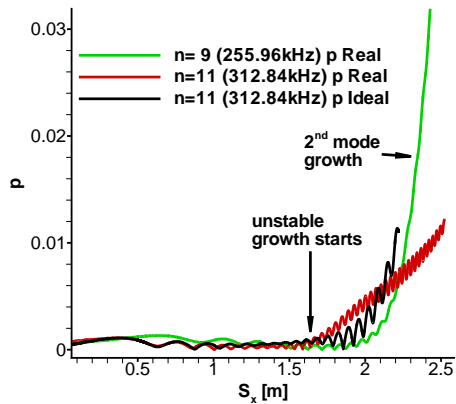


(f) $n=9$

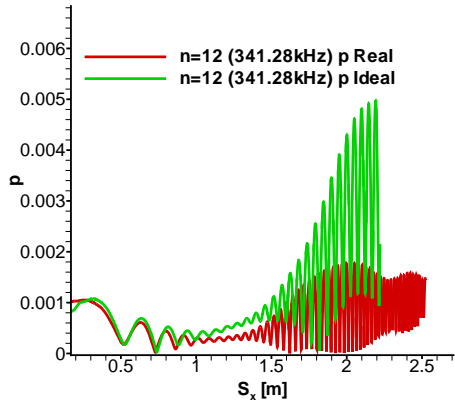
Figure 27. Comparison of pressure perturbation amplitudes. Contd. next pg. ...



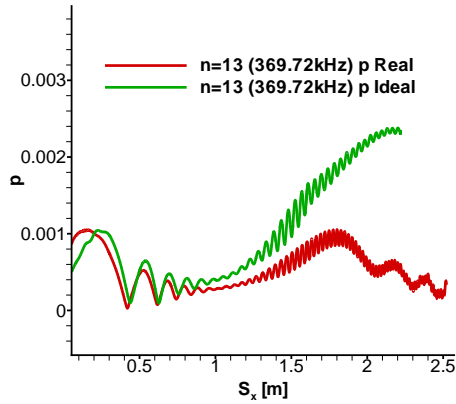
(g) $n=10$



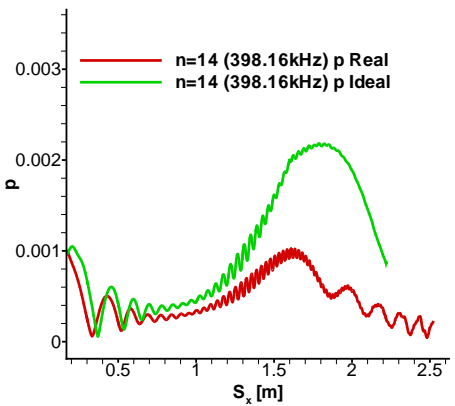
(h) $n=11$



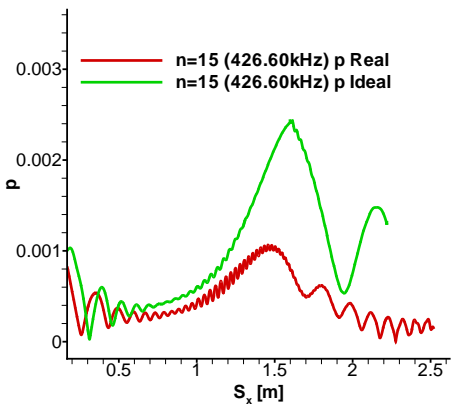
(i) $n=12$



(j) $n=13$



(k) $n=14$



(l) $n=15$

Figure 27. Comparison of pressure perturbation amplitudes. Contd. next pg. ...

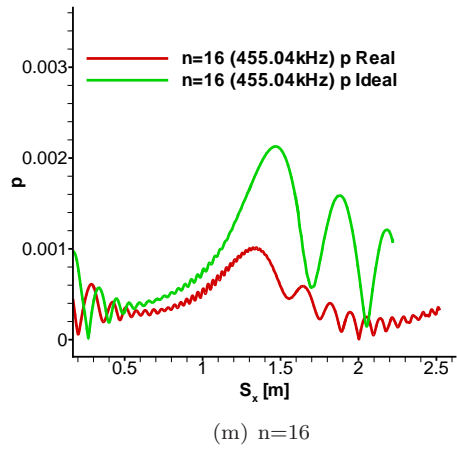
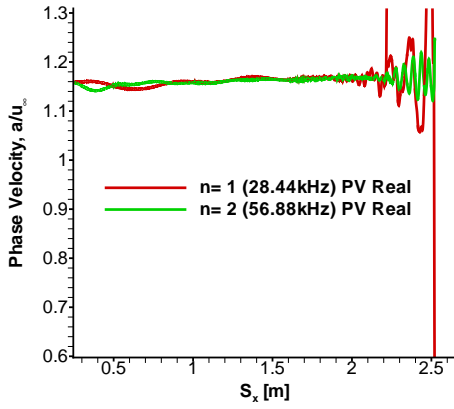
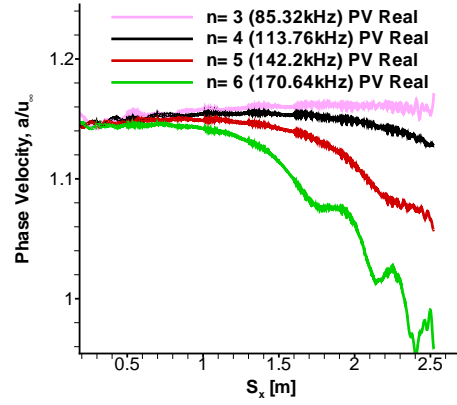


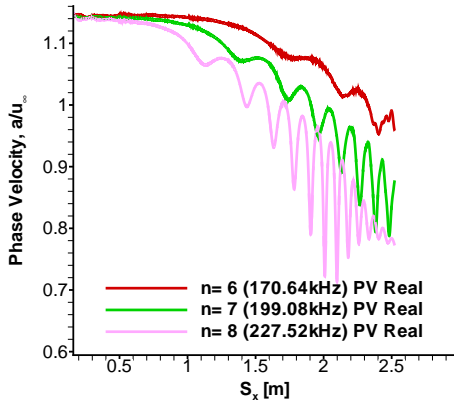
Figure 27. Comparison of pressure perturbation amplitudes ideal (light lines) and real (dark) gas simulations for frequencies $n=1$ to $n=16$.



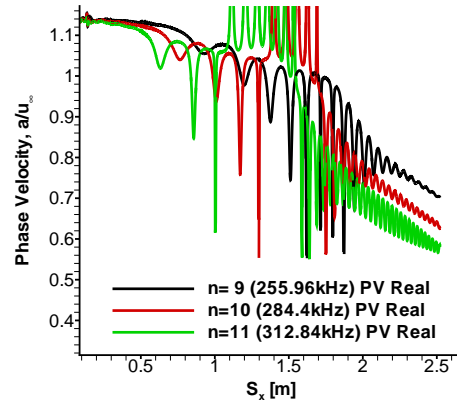
(a) n=1,2



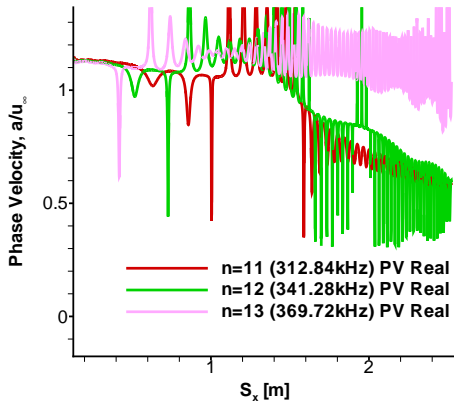
(b) n=3 to 6



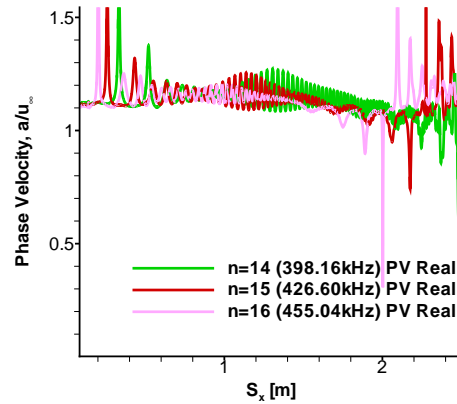
(c) n=6 to 8



(d) n=9 to 11

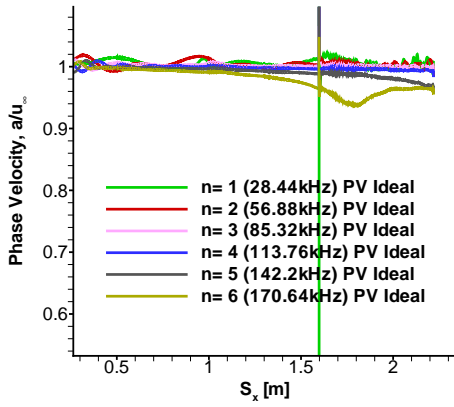


(e) n=11 to 13

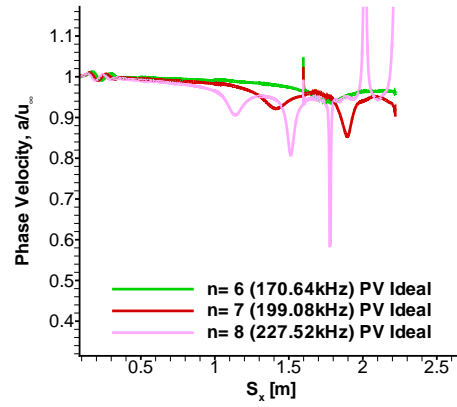


(f) n=14 to 16

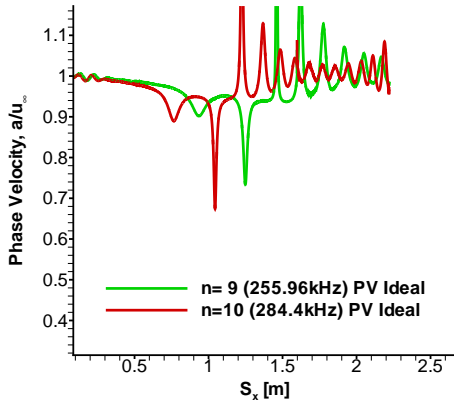
Figure 28. Phase velocity vs Natural Coordinate for frequencies n=1 to n=16, Real gas simulations.



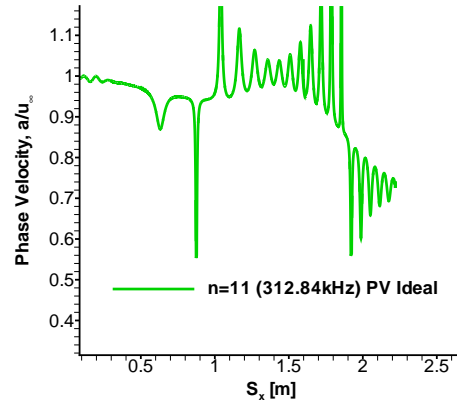
(a) n=1 to 6



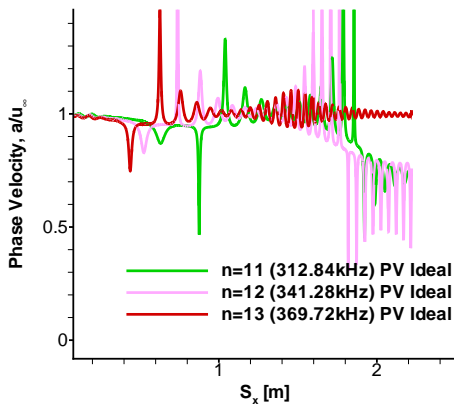
(b) n=6 to 8



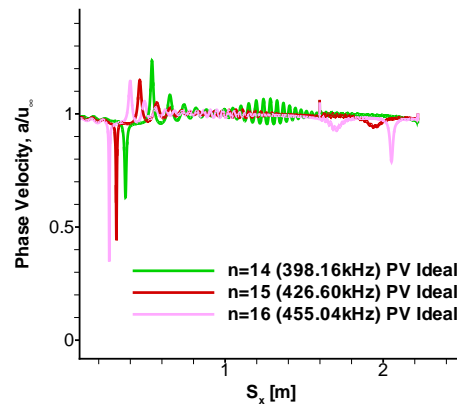
(c) n=9 to 10



(d) n=11



(e) n=11-13



(f) n=14-16

Figure 29. Phase velocity vs Natural Coordinate for frequencies n=1 to n=16, Ideal gas simulations.